Hindawi
Advances in Civil Engineering
Volume 2023, Article ID 7431867, 22 pages
https://doi.org/10.1155/2023/7431867

Research Article

Structural Condition Assessment and Temperature Effect Analysis of Cable–Pylon Anchorage Zone Using Long-Term SHM Data

Hanhui Ye[1] **and Zhijian Chen**[2]

[1]*College of Civil and Transportation Engineering, Hohai University, Nanjing 210098, China*
[2]*School of Earth Sciences and Engineering, Hohai University, Nanjing 210098, China*

Correspondence should be addressed to Hanhui Ye; 1072193393@qq.com

Received 18 October 2022; Revised 29 June 2023; Accepted 14 July 2023; Published 8 August 2023

Academic Editor: Ahad Javanmardi

To study the temperature effect in the anchorage zone of a long-span cable-stayed bridge, a wavelet multiresolution analysis and layered stripping method were used in this paper. Based on long-term structural health monitoring data, the signals were decomposed and reconstructed at multiple time scales, confirming temperature to be the main factor causing the stress change in the anchorage zone. The results of structural condition during operation showed that the general compressive stress level of the anchorage zone was low. However, the tensile stress level of the sidewall was high, which led to a severe concrete cracking. Excluding the influence of the seasonal temperature, the compressive stress increased slightly, the horizontal tensile stress in the upstream inner pylon wall increased, and the crack width increased gradually. By analysing the daily temperature effect on the upstream and downstream pylon walls, the regression model proposed in this study can be used to predict the daily temperature effect at any time in the diurnal cycle. The accuracy of the model is reliable within 6 days, but for the location of severe cracks, the monitoring data should be updated in real time to ensure the precision.

1. Introduction

The cable force and cable pylon height increase with the span of a cable-stayed bridge. The cable pylon is in a state of compressive and bending stress, and mainly bears the axial force. The self-weight of the superstructure and external load borne by the anchorage structure are transferred to the cable pylon. Except for a few steel pylons, most long-span cable-stayed bridges use concrete pylons with thin-walled hollow sections [1].

Anchoring forms of concrete cable pylons in long-span cable-stayed bridges include prestressed reinforcement, steel anchor beam, steel anchor plate, and steel anchor box anchorings. Because steel is prone to instability under a larger compressive stress, and concrete is prone to cracking under a larger stress, owing to the steel anchor box anchor structure, the steel can share a larger horizontal component, while concrete bears a larger vertical component and smaller tensile force, which improves the bearing capacity of the anchoring area. This is a reasonable structure form that does not require the installation of prestressed steel bundles. Therefore, it has been widely used in construction of long-span cable-stayed bridges in recent years [2, 3].

The structure of the cable–pylon anchorage zone is complex, the stress is concentrated, and its internal force, deformation, and stress distribution are difficult to accurately analyze. Many scholars have studied the mechanical mechanism and properties of anchorage structures. The steel anchor box transmits most of the vertical component of the stay cable to the concrete pylon through shear nails or shear connection keys, which can prevent the superposition of vertical forces at the bottom of the steel anchor box and thus prevent stress concentration [4]. The horizontal component of the cable force is the controlling factor for the force in the anchorage zone [5]. The most disadvantageous position of the steel box anchor is the concrete pylon wall in the transverse bridge direction [5, 6]. The defects in the segmental model test include the limitations of the model height and

influence of the boundary conditions. The stress of the concrete in the test model is not uniform in the height direction, whereas the stress of the pylon wall is different from that of the real structure [7]. Numerical results of a finite-element analysis are in a good agreement with those of the section test. The stress and displacement values of the single-section model are larger than those of the multisection model [8].

For a real bridge in a natural environment, the actual stress condition of the cable–pylon anchorage zone is highly sensitive to external constraints and local deformation. Moreover, because the cable–pylon is affected by solar radiation, day and night alternation, seasonal change, cold wave cooling, and other bad weather conditions throughout the year, the adverse structural temperature field leads to a considerable temperature stress in the anchorage zone. Nie et al. [9] considered the most unfavorable temperature field and analyzed the stress in the anchorage zone of a cable–pylon with a circumferential prestressed anchoring using the finite-element method. Li and Cai [10] analyzed the temperature effect caused by a temperature change or uneven temperature in the cable–pylon anchorage zone using the finite-element method and obtained the temperature stress distribution under the action of the corresponding temperature field. Li et al. [11] established a solar temperature field calculation model for a cable–pylon and used Hong Kong–Zhuhai–Macao Bridge as an example to verify the effectiveness of the model. Fan and Qian [12] used an indirect coupling method to effectively combine the temperature load with other load stress fields to obtain an accurate stress distribution on a cable–pylon structure.

The design and operational life of long-span bridges is approximately 100 years. As a comprehensive bridge test, structural health monitoring (SHM) can monitor the responses of bridges under real loads and real environments during the operation period and is widely used in studies on the temperature effects of steel box girders, concrete box girders, steel trusses, and steel–concrete composite beam [13–18]. The distributed SHM data can effectively capture the relationship between the temperature distribution and structural response, which has a high-practical engineering value. In contrast, only a few scholars have studied the temperature effect of cable–pylons based on SHM data. Zhou et al. [19] used Wangdong Yangtze River Highway Bridge as a background, and based on temperature data from the health monitoring system during a period of 1 year, a calculation model was presented for the temperature gradients of the cable–pylon. Yang et al. [20] studied the time variability of the thermal field distribution and pylon displacement based on measured temperature and displacement data. Xu et al. [21] proposed a practical model based on linear variables for the modeling and separation of the thermal effects of cable-stayed bridge responses. Jin et al. [22] obtained the relative relationship between the cable–pylon crack width and temperature difference through an analysis of field observation data. The main problems in these studies are as follows: (1) short monitoring time, insufficient number of monitoring points, and low degree of matching between the method and structural behavioral characteristics; (2) the analysis of temperature effects only considers the most adverse effects without studies on different timescales; (3) the research on the nonlinear behavior of temperature-induced responses is insufficient. Complex structures and environments usually lead to a high degree of nonlinearity.

In terms of the SHM data interpretation methods for temperature effect studies, Kromanis and Kripakaran [23, 24] proposed a regression-based thermal response prediction method and temperature-based measurement interpretation method. Wang et al. [14] proposed an improved Bayesian dynamic linear model, in which the trend, season, regression, and autoregressive components were considered. Real-time monitoring data collected from long-span cable-stayed bridges demonstrate the feasibility of the method, which allows a probabilistic prediction and thus provides a large amount of information regarding the temperature-induced strain response. Zhao et al. [25] proposed a distribution mapping method by analyzing the data characteristics of long-term time series. Wu et al. [26] used a wavelet transform to extract the temperature change component with a higher cutoff frequency in the strain data. Xu et al. [27] proposed a method based on a multiresolution wavelet to extract thermal effects from bridge responses at different frequency bandwidths. Wang et al. [28] proposed a time–frequency analysis method that combined the wavelet threshold denoising algorithm, which was verified by health monitoring data from Sutong Bridge, and proved that the method is suitable for a nonstationary signal processing with noise. Huang et al. [29] studied the temperature response of the deflection of a cable-stayed bridge with the third bridge of Nanjing Yangtze river as an object and analyzed the time and multiscale characteristics of the long-term deflection monitoring signal. The deflection signal was reconstructed on two scales (daily period and annual period) using the wavelet multiscale analysis method to separate the temperature effect. Zhao et al. [30] identified the beam deflection caused by the temperature and train through a wavelet packet analysis, and used a window with threshold to automatically extracted the nonstationary part of the train induced response [31]. These results show that the effect of the algorithm is determined by the structural properties, number of samples, and quality of the collected data. The dataset must include the full range of variability in the measurements, which, for a full-size structured study on temperature effects, implies that at least 1 year of measurements is required to ensure the validity of the results. Most algorithms still have some weaknesses, such as poor data fusion analysis ability and timeliness and low applicability of performance evaluation from theoretical methods to practical applications. Based on the multiscale theory of wavelet transform, a wavelet multiresolution analysis can be used to directly analyze measured time series data. Compared to other data-driven algorithms, it can decompose and reconstruct response signals at different time scales. Therefore, it has natural advantages in processing phenomena or processes with multiscale characteristics.

Based on the above analysis, in this study, we use the long-term SHM data (5.5 years, 27 monitoring points) of the cable–pylon anchorage zone of Sutong Bridge to study the stress characteristics of the cable–pylon anchorage zone under real loads and environments during operation and

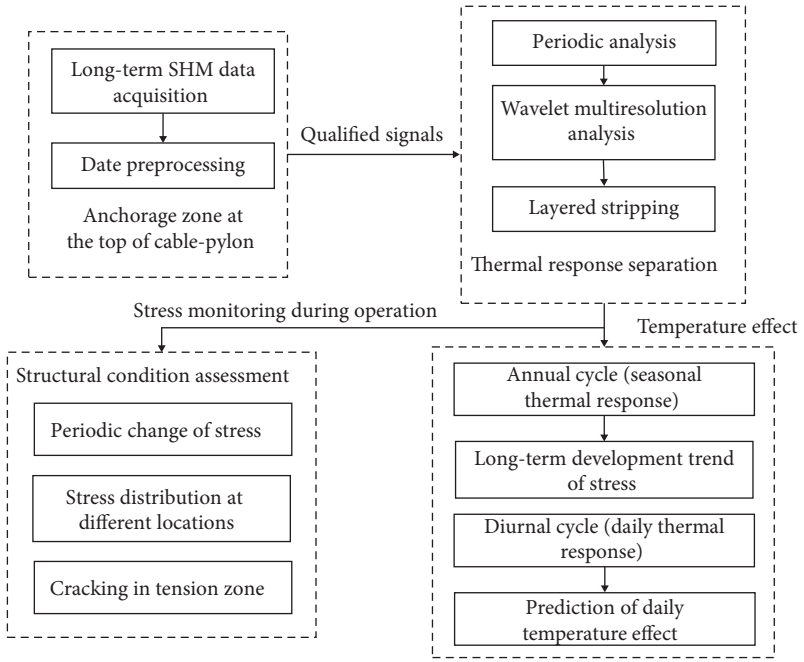

Figure 1: Flowchart of the methodology.

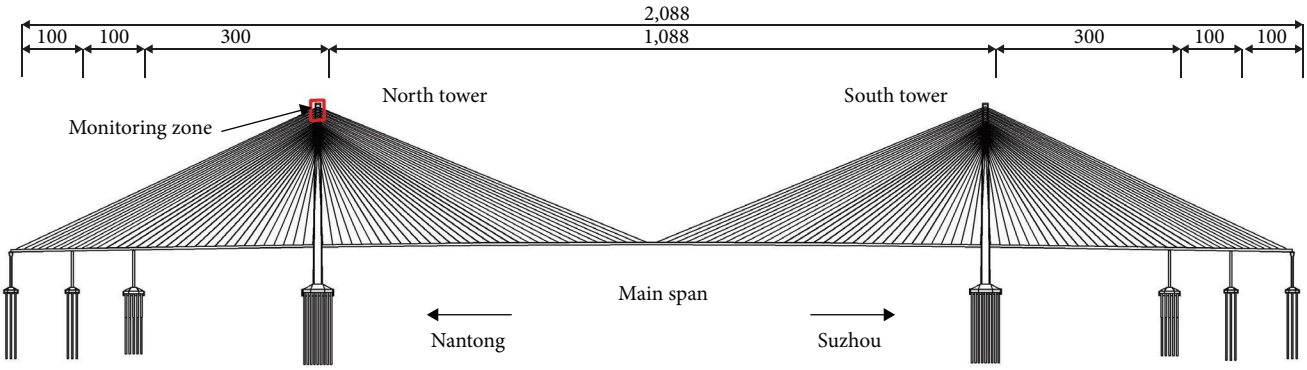

Figure 2: Layout of Sutong Bridge (unit: m).

stratify the temperature effects at different time scales through a wavelet multiresolution analysis. The main objectives are as follows: (1) according to the annual temperature effect, the long-term development trend of stress and condition of the unfavorable stress area are analyzed, and the structural condition of the top anchorage zone during operation is evaluated; (2) based on the analysis of the daily temperature effect, the relationship between the temperature and strain response is analyzed, and a corresponding regression model is proposed to predict the daily temperature effect at any time in the daily cycle. A flowchart of the specific method used in this study is shown in Figure 1.

2. Cable–Pylon Anchorage Zone and Monitoring Point

2.1. Overview of the Bridge and Cable–Pylon Anchorage Zone. Sutong Bridge is located at the estuary of Yangtze River in southeast Jiangsu Province. The axis of the bridge is 10.6° north by east. The bridge is located in the north subtropical humid monsoon area, with an average annual temperature of 15.4°C. The annual extreme maximum and minimum temperature are 42.2 and −12.7°C, respectively. The main span of the bridge employs an inverted Y-shaped pylon. The total height of the pylon is 300.40 m and the height-to-span ratio is 0.212. The upper pylon consists of a single box and single chamber. The outer dimensions change from 900×800 to $1{,}080 \times 1{,}740$ cm^2. The wall thickness is 100 cm on the anchorage surface and 120 cm on the nonanchorage surface. Stay cables (34 pairs) are arranged on each side of the pylon, of which four pairs on each bottom side (cable no. 1–4) are anchored on the beam of the pylon, and the remaining 30 pairs on each side (cable no. 5–34) are anchored in steel anchorage boxes [2, 3]. The layout of Sutong Bridge is shown in Figure 2.

Because the intersection angle between the cable and horizontal direction gradually increases from top to bottom,

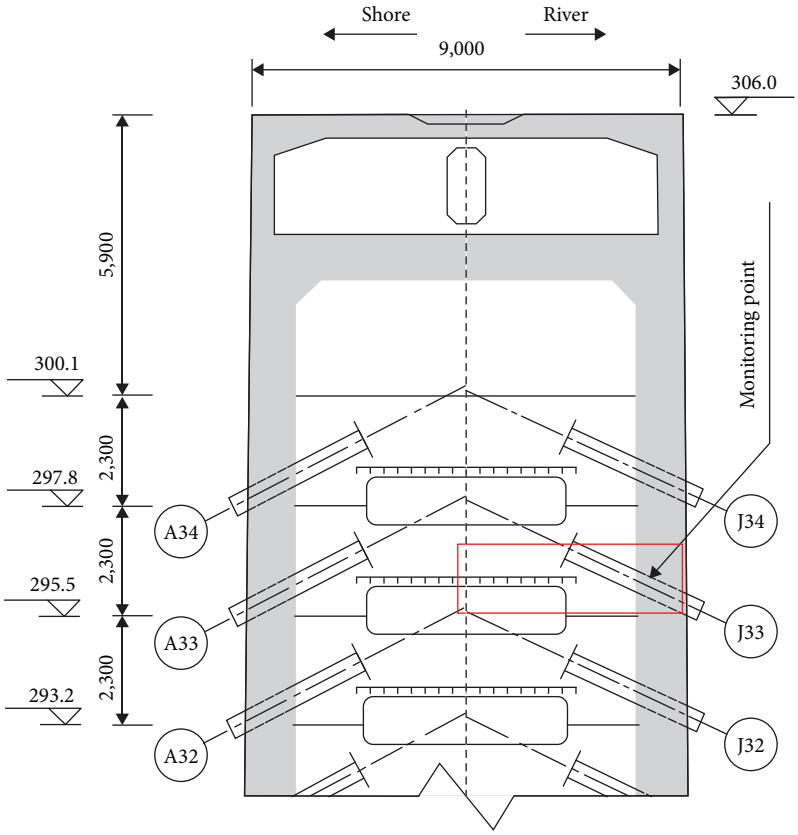

Figure 3: Anchorage zone at the top of the cable–pylon (elevation unit: m, length unit: mm).

and the cable force gradually decreases from top to bottom, the steel anchor box and concrete at the top segment are subjected to the highest tension in the horizontal direction. Therefore, the anchorage zone at the top of the cable–pylon is selected for this study, as shown in Figure 3.

Considering that the side pull plate of the J34 steel anchor box is slotted only on one side, and the top structure of the cable–pylon has a certain influence on the concrete stress of the pylon wall, the stress monitoring point is selected in the anchorage zone of J33. Based on the symmetry of the steel anchor box structure and force, the monitoring points of the anchorage zone are concentrated in the downstream half of the riverside. The structure of the elevation plane section of the top anchorage zone (J33) is shown in Figure 4. The details of the steel anchor box structure and arrangement of the monitoring points are shown in Figure 5.

2.2. Monitoring Point Arrangement. The strain and temperature of the monitoring points are measured by BGK-4200 vibrating string concrete strain gauge equipped with semiconductor thermometer, and the monitoring data are automatically collected by BGK-MICRO40 data acquisition instrument. The specific arrangement of the monitoring points in the cable–pylon anchorage zone is shown in Figures 6–11. The locations of monitoring points are listed in Table 1.

The distance in Table 1 refers to the vertical distance between the monitoring point and three planes that are perpendicular to each other. For the monitoring points arranged on the riverside, the three planes are undersurface of the bottom plate, external surface of the end plate, and symmetry plane (longitudinal bridge). For the monitoring points

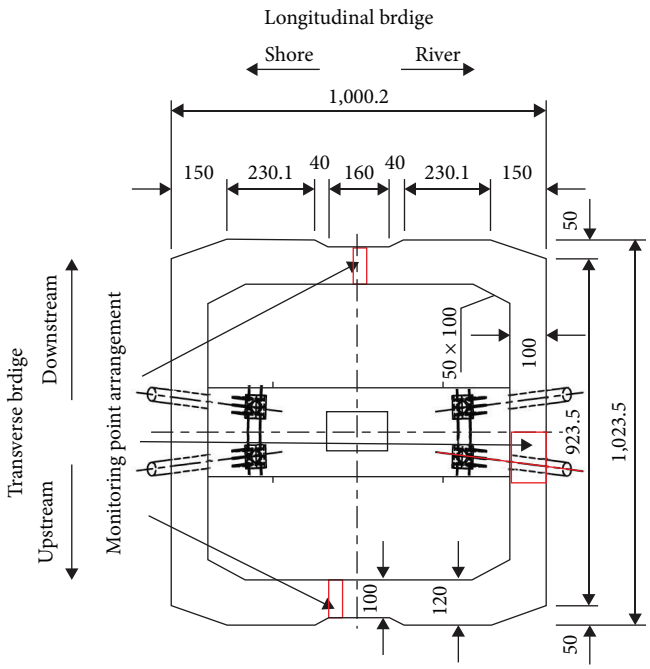

Figure 4: Structure of the elevation plane section of the top anchorage zone (unit: cm).

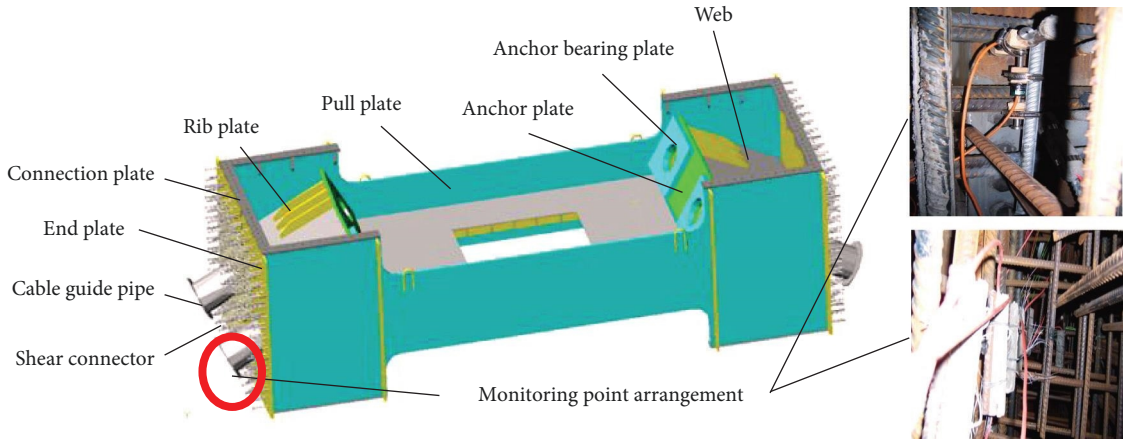

Figure 5: Steel anchor box structure and monitoring point arrangement diagram.

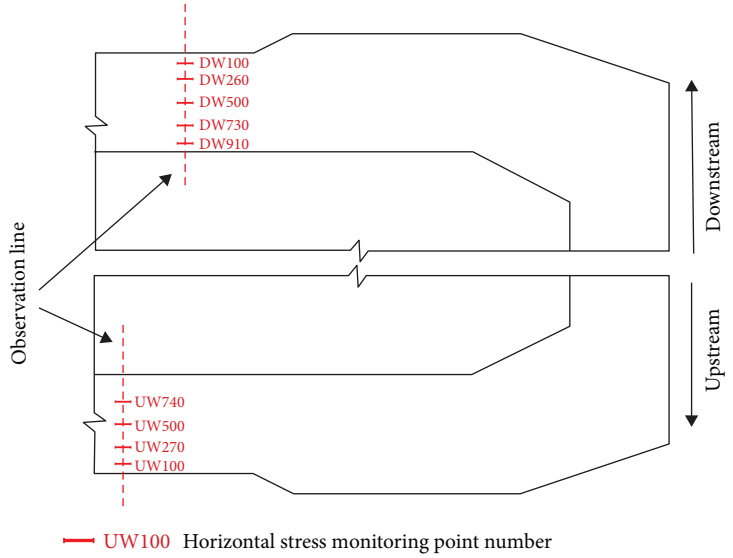

Figure 6: Layout of monitoring points on the walls of the upstream and downstream pylons.

arranged on the upstream and downstream pylon walls, the three planes are undersurface of the bottom plate, symmetry plane (transverse bridge), and upstream or downstream outer pylon wall.

As shown in Table 1, E1–E7 are located near the end plate on the transverse bridge section. N1–N5 are located near the shear connector cap in the transverse bridge section. E1, N1, U1, U2, and U3 are located at the upstream edge of the steel anchor box on the longitudinal bridge section. C2, E7, C1, N5, and A1 are located near the symmetry plane (longitudinal bridge).

The monitoring points on the upstream and downstream pylon walls have the same height and are organized in the form of observation lines, as shown in Figure 6. DW100, DW260, DW500, DW730, and DW910 are located at the downstream pylon wall. UW100, UW270, UW500, and UW740 are located upstream of the pylon walls. UW and DW stand for the abbreviations of upstream and downstream pylon walls, respectively. Different numbers indicate the vertical distance (mm) from the monitoring point to the outer pylon wall.

3. Methods and Theory

3.1. Multiresolution Analysis (MRA). Wavelet transform divides a signal into an approximate subspace containing a low-frequency decomposition information (coarse resolution) and a detailed subspace that stores a high-frequency component information (high resolution). The former retains the primary features of the original signal and the latter reflects the detailed features of the original signal. MRA is a theory based on the concept of function space, which refers to the combination of wavelet transform and filter. According to the frequency bandwidth, the energy-limited signal space is divided into nested subspaces. The decomposition algorithm and specific bandwidth are shown in Figure 12.

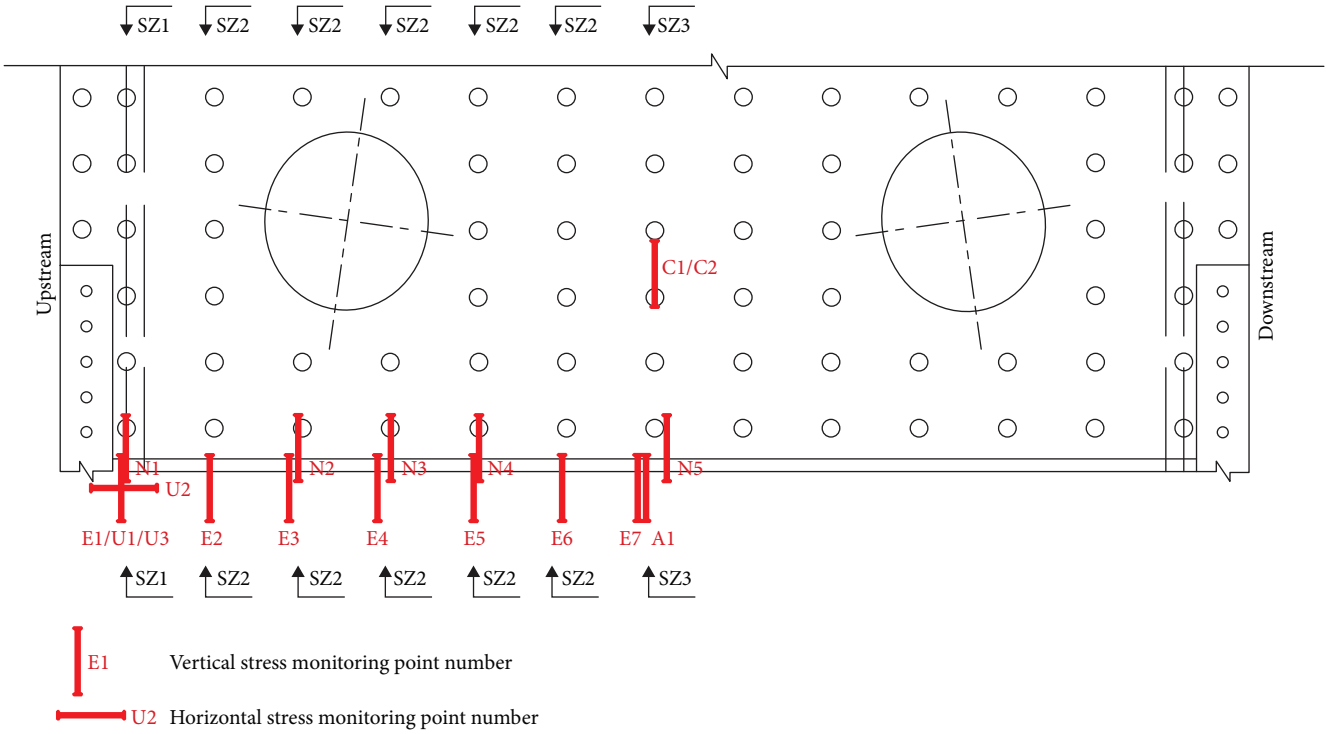

Figure 7: Elevation view of the monitoring points in the top anchorage zone.

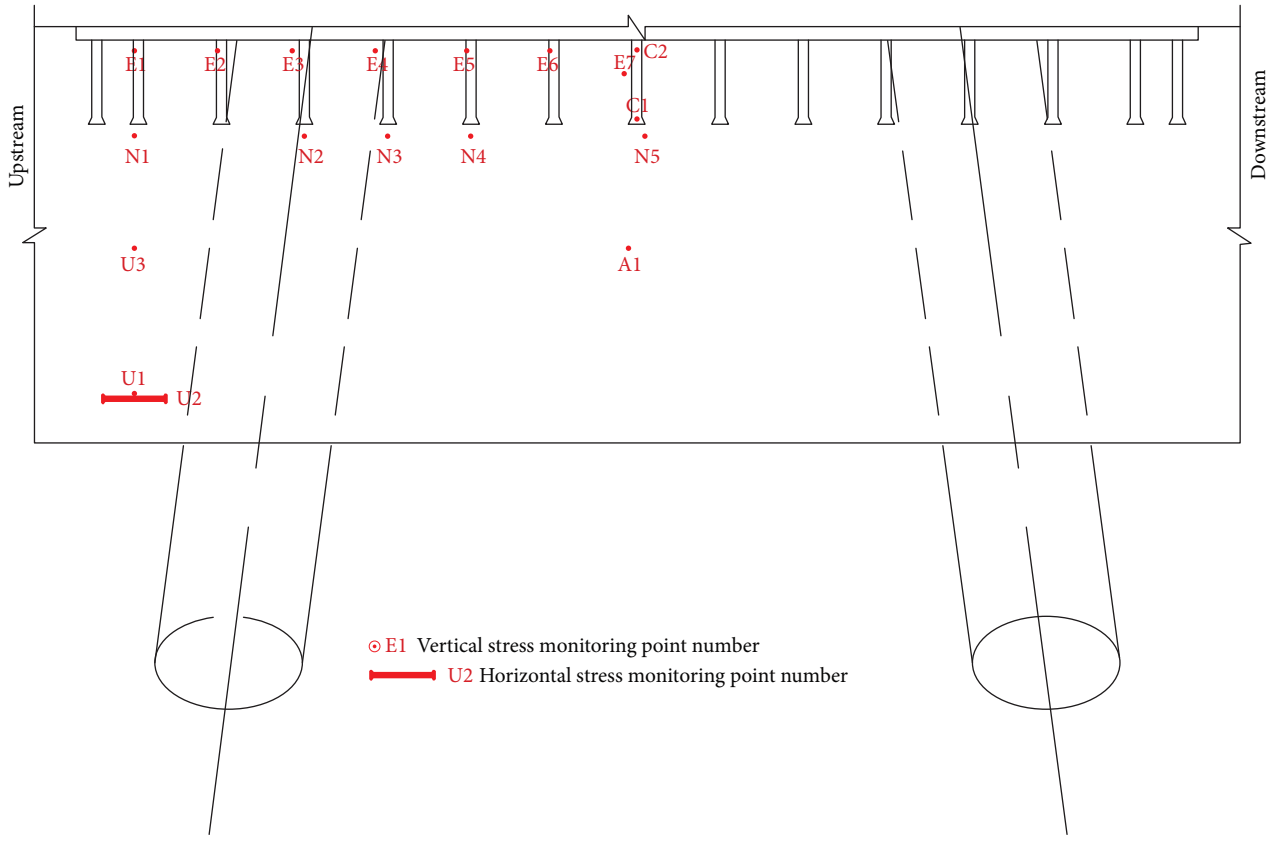

Figure 8: Top view of the monitoring points in the top anchorage zone.

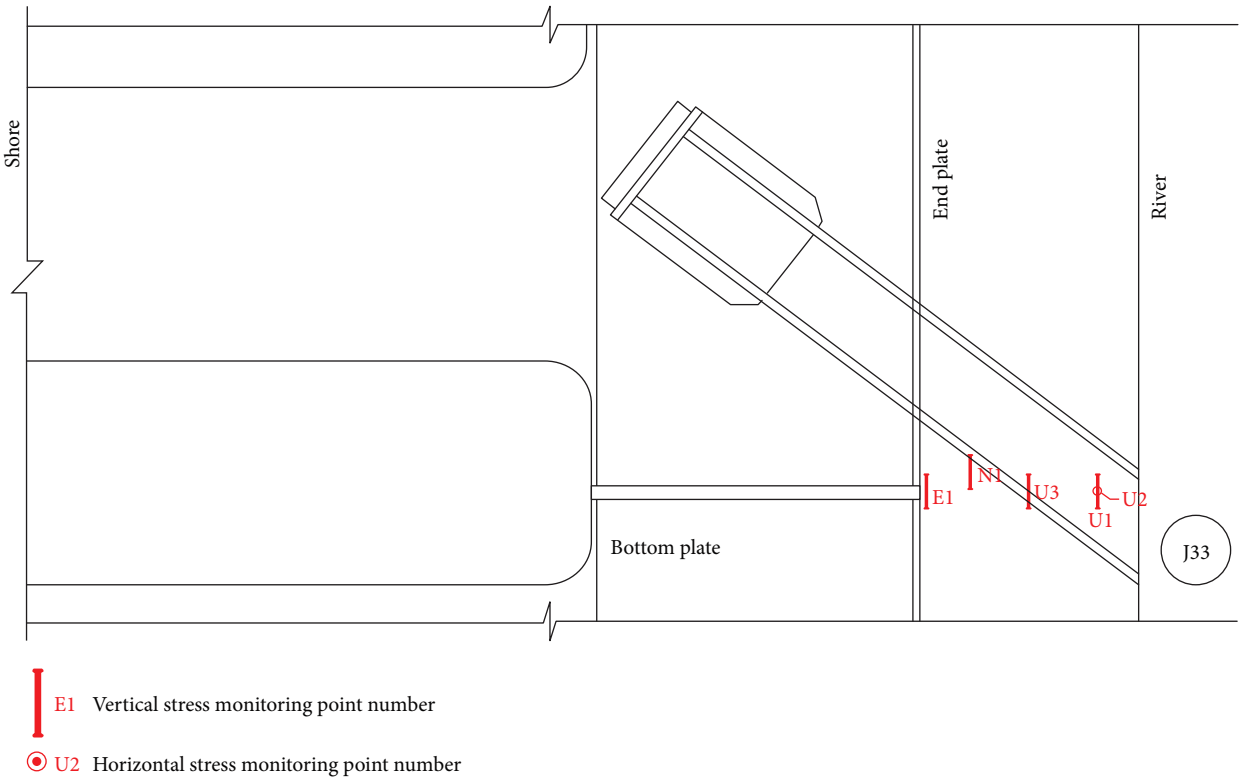

Figure 9: Sectional view (SZ1) of the monitoring points in the top anchorage zone.

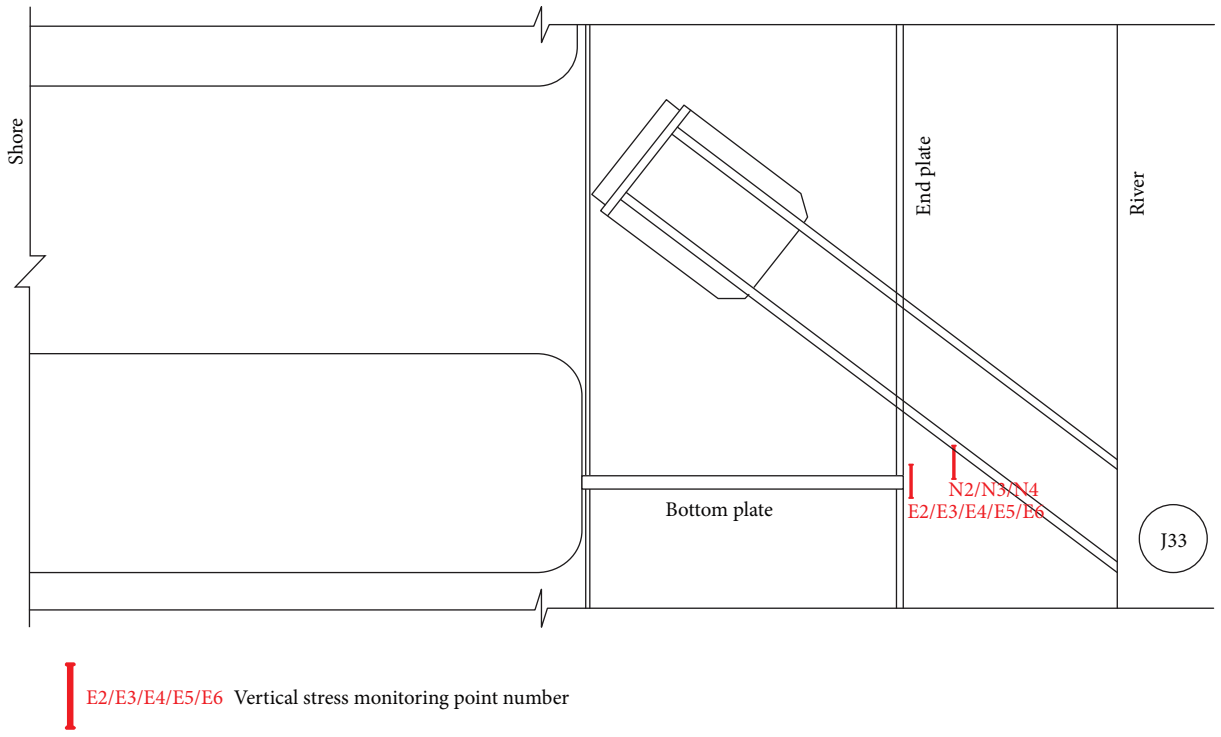

Figure 10: Sectional view (SZ2) of the monitoring points in the top anchorage zone.

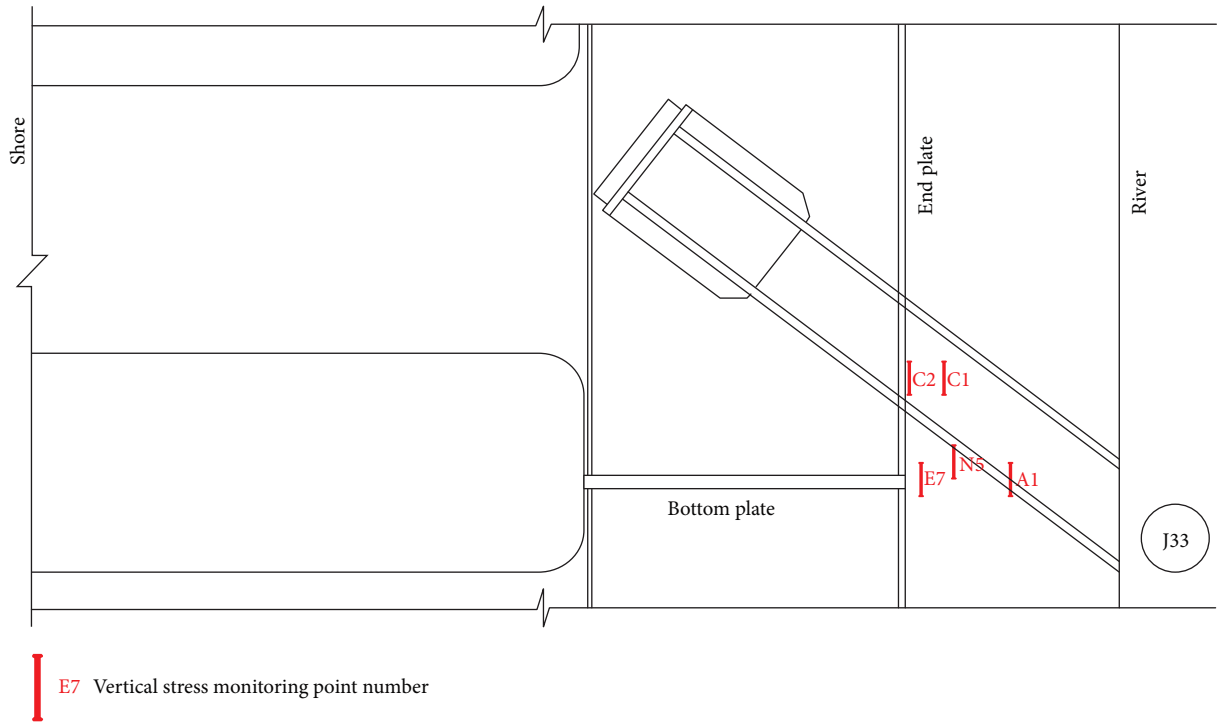

Figure 11: Sectional view (SZ3) of the monitoring points in the top anchorage zone.

Table 1: Specific locations of the monitoring points.

Monitoring point number	Vertical distance from the monitoring point to the plane (mm)		
	Undersurface of the bottom plate	External surface of the end plate or the symmetry plane (transverse bridge)	The symmetry plane (longitudinal bridge) or the outer pylon wall
E1	30	25	1,260
E2			1,060
E3			880
E4			680
E5			460
E6			260
E7		80	80
N1	120	230	1,260
N2			850
N3			650
N4			450
N5			30
A1	30	500	70
U1		850	1,260
U2		850	
U3		500	
C1	383	190	0
C2		25	
UW100	383	600	100
UW270			270
UW500			500
UW740			740
DW100			100
DW260			260
DW500		30	500
DW730			730
DW910			910

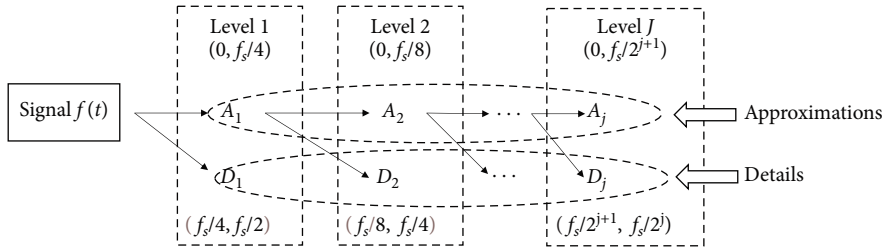

Figure 12: Decomposition algorithm and bandwidth division diagram.

The full expanding of discrete signal $f(t)$ at the Jth level can be expressed as follows:

$$f(t) = A_J(t) + \sum_{j=1}^{J} D_j(t), \tag{1}$$

$$A_j(t) = \sum_{k \in Z} C_{j,k} \varphi_{j,k}(t), \tag{2}$$

$$D_j(t) = \sum_{k \in Z} D_{j,k} \psi_{j,k}(t). \tag{3}$$

Substituting Equations (2) and (3) into Equation (1) is obtained as follows:

$$f(t) = \sum_{k \in Z} C_{J,k} \varphi_{J,k}(t) + \sum_{j=1}^{J} \sum_{k \in Z} D_{j,k} \psi_{j,k}(t), \tag{4}$$

where $C_{j,k}$ is the approximation coefficient and $D_{j,k}$ is the detail coefficient at the jth level. $\varphi_{j,k}(t)$ is the scaling function and $\psi_{j,k}(t)$ is the wavelet function. For a given sample frequency f_s, the maximum recognition frequency of a signal is $f_s/2$ according to Nyquist–Shannon sampling theorem. $A_j(t)$ is the component of $f(t)$ for which frequency does not exceed $f_s/2^{j+1}$, whereas $D_j(t)$ is the component with frequency between $f_s/2^{j+1}$ and $f_s/2^j$. When $f(t)$ is reconstructed, the part D_j related to the noise is removed, and the filtered smooth signal $\tilde{f}(t)$ can be obtained.

The number of decomposition layers can be determined by gradually increasing the number of layers and determining whether the change in the root-mean-square error (RMSE) stabilizes. When the number of decomposition layers is $k = 1, 2, 3\ldots$, the RMSE between the original and estimated signals is defined as follows:

$$RMSE(k) = \sqrt{\frac{1}{n} \sum_{n} \left[f(n) - \hat{f}(n) \right]^2}. \tag{5}$$

3.2. Periodicity Analysis. The strain and temperature data used in this study are obtained from the SHM system installed in the cable–pylon anchorage zone of Sutong Bridge. The result from the SHM is a discrete set of data with a sampling period of 3 hr (frequency of 1/10,800 Hz). Taking DW260 as an example, the 1 year monitoring data (2012/10/1–2013/9/30) are shown in Figure 13 (a data point on the X-axis represents one sampling). In addition, fast Fourier transform was performed on the measured strain and temperature in Figure 13 to obtain the spectrum diagram shown in Figures 14 and 15 (3 hr is considered as 1 s for the frequency unit).

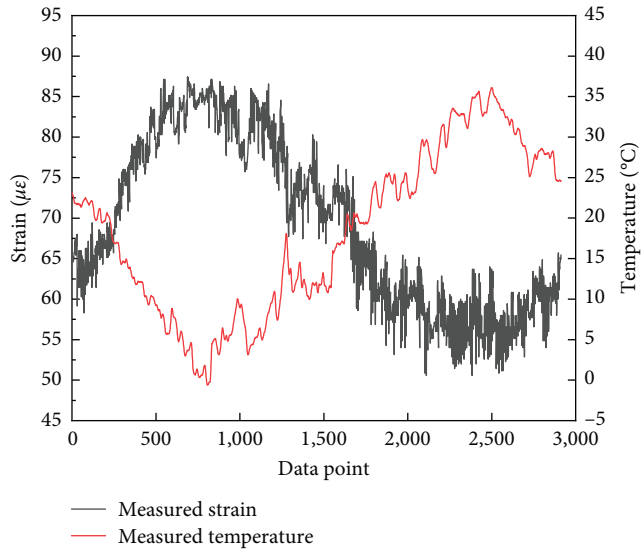

Figure 13: One-year measured strain and temperature.

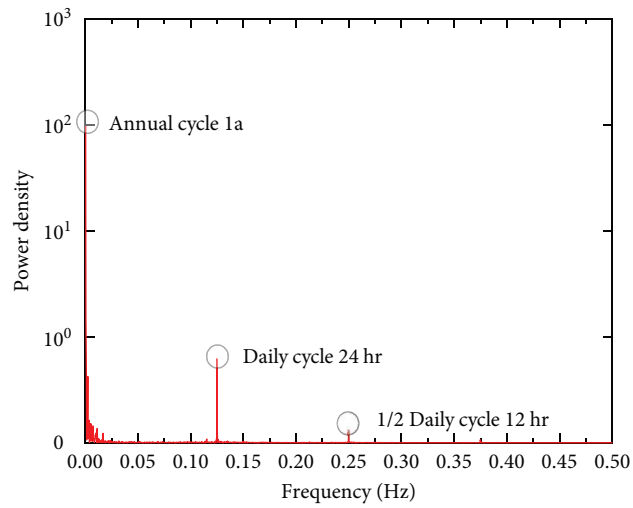

Figure 14: Spectrum diagram of the measured strain.

Figures 14 and 15 show that the spectrum diagrams of the temperature and strain signals have three obvious concentrated amplitudes in the low-frequency region below 0.25 Hz. The corresponding frequencies are approximately

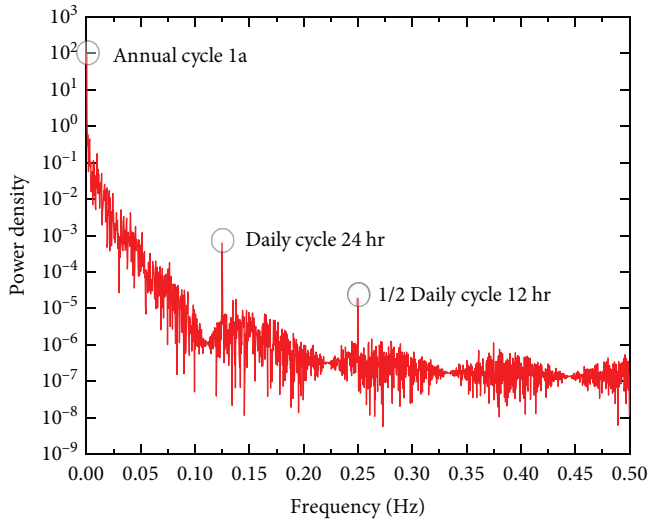

Figure 15: Spectrum diagram of the measured temperature.

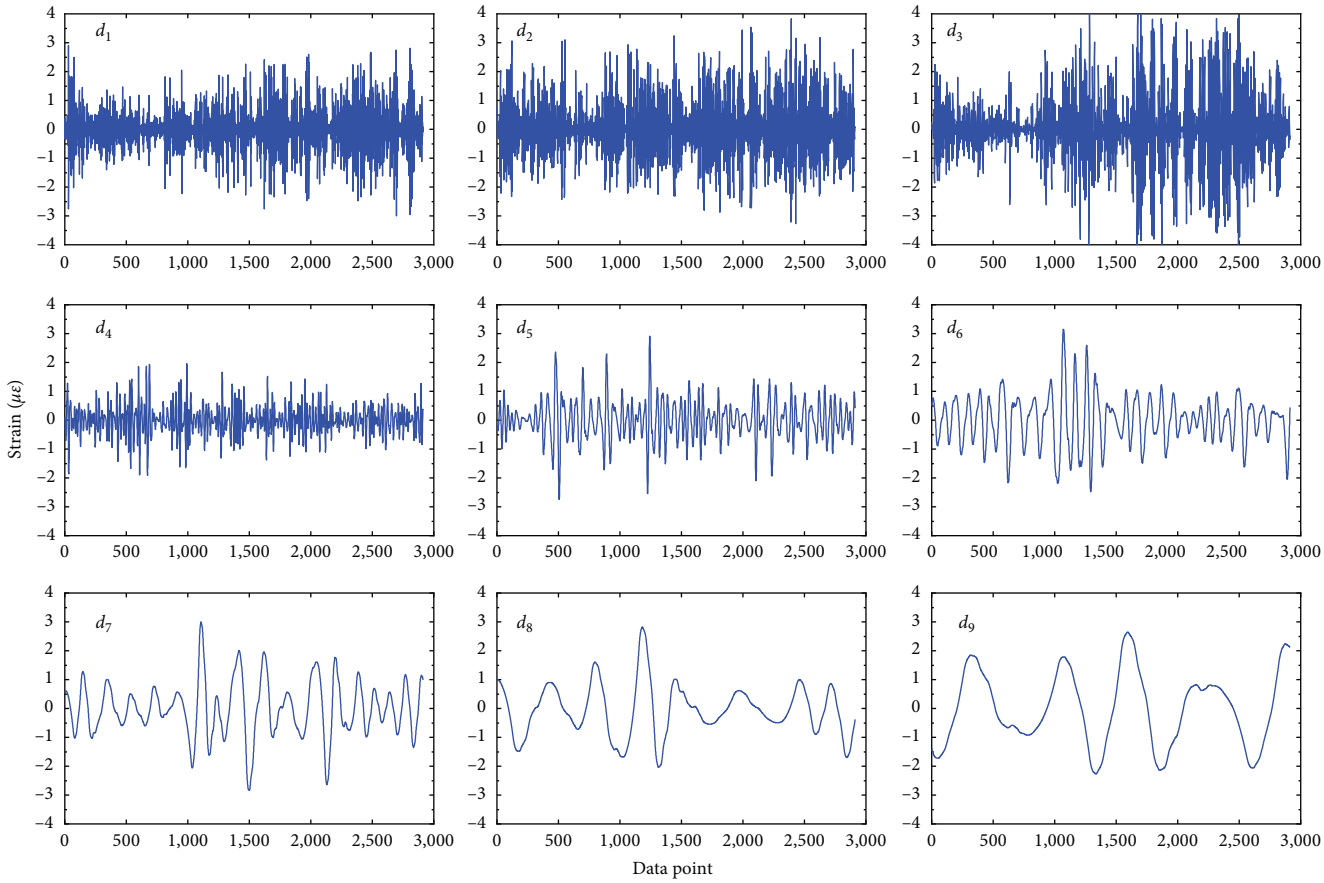

Figure 16: Layers of details obtained after the nine-layer decomposition.

3.42×10^{-4}Hz (annual period), 1.25×10^{-2}Hz (daily period), and 2.50×10^{-2}Hz (1/2 daily period). Periodic temperature changes causes periodic fluctuations in the measured strain. Such periodic fluctuations include small-scale fluctuations caused by solar radiation and diurnal temperature differences as well as large-scale fluctuations caused by seasonal temperature changes.

3.3. Layered Stripping. The temperature variation in the large-scale period is regular, whereas that in the small-scale period varies. The form and amplitude of the response caused by different temperature changes are considerably different. According to the conditions of the bridge operation period and environmental climate conditions, the effects of temperature changes on different scales were separated step

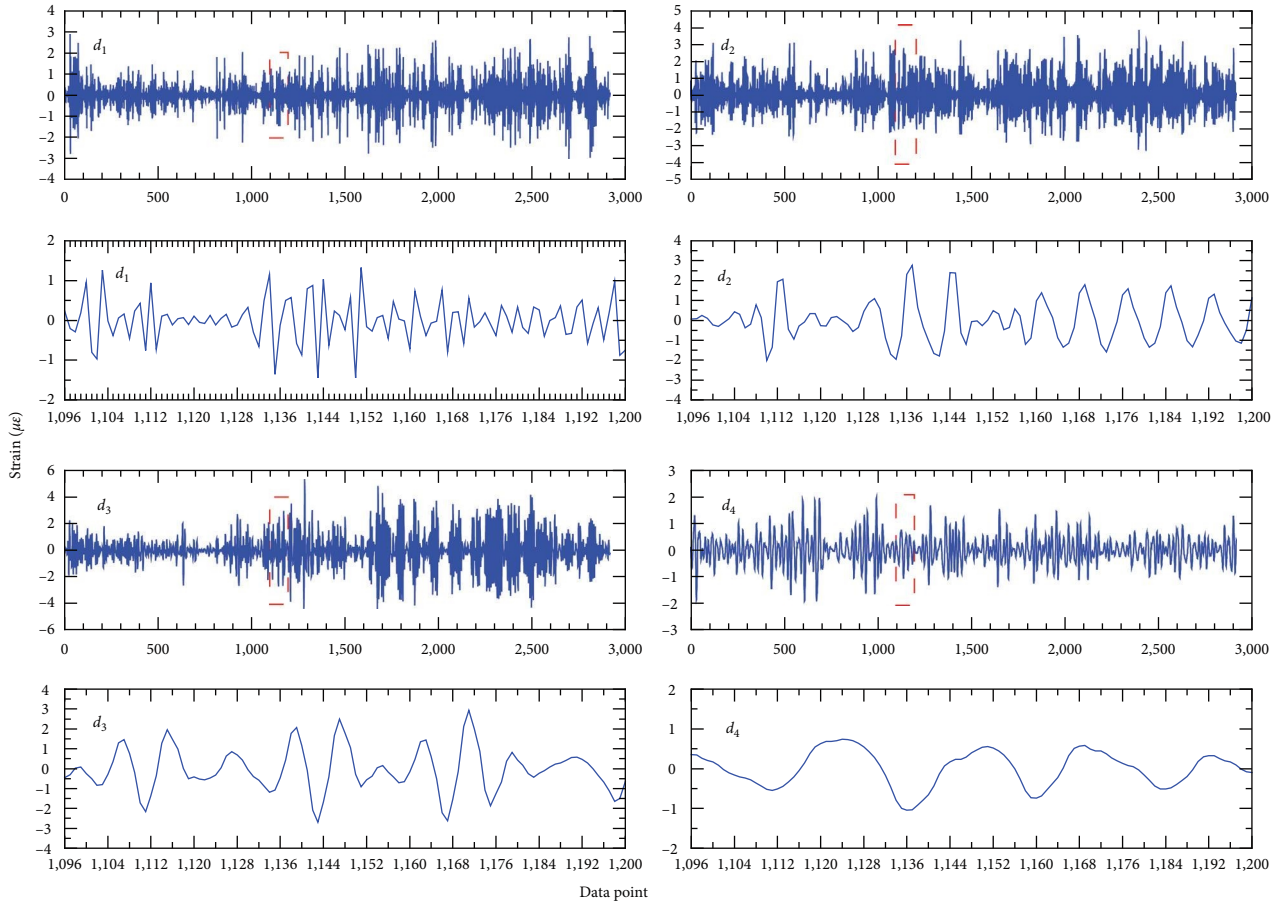

FIGURE 17: Details of the first four layers and their local magnification.

by step according to the differences between the responses of different layers in different periods. Considering the measured strain data in Figure 13 as an example, the detailed parts of each layer obtained after a nine-layer decomposition are shown in Figure 16. Figure 17 shows the details of the first four layers and partial enlargement.

As shown in Figures 16 and 17, the period of d_1 can be considered to be shorter than the sampling period of the monitoring system. The response includes the influence of solar radiation, vehicle load, and other high-frequency factors. The period of d_2 is 24 hr and is attributed to the difference in temperature between day and night. The period of d_3 is close to 24 hr and is attributed to the temperature difference at the specific time (sampling time of the sensor) between different days. The periods d_4– d_9 are between the diurnal and seasonal thermal responses. Although the period gradually increases, the amplitude of the response is approximately of the same order of magnitude. The data in Figure 13 are layer stripped to obtain the strain that retains the seasonal thermal response and strain that excludes the seasonal thermal response, as shown in Figure 18.

Figure 18 shows the applicability and effectiveness of the layered stripping method for processing of long-term SHM data. After the exclusion of short-period and occasional factors, the influence of the seasonal continuous temperature increase and decrease on the structural response is more intuitive.

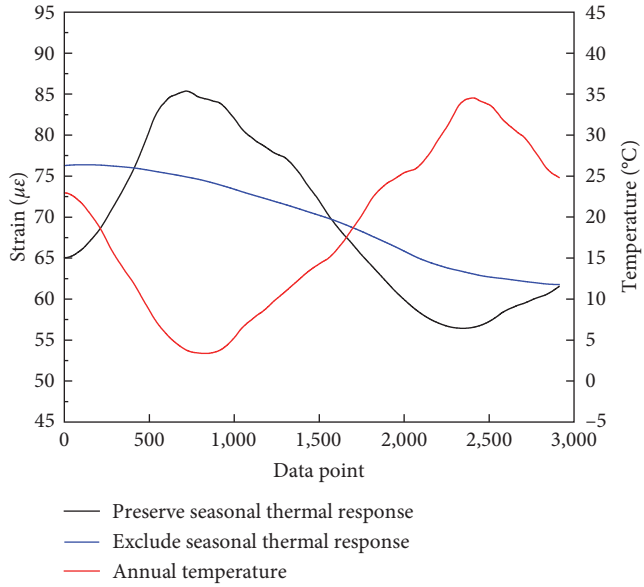

FIGURE 18: Preservation or exclusion of seasonal thermal response strains.

Additionally, more information can be obtained using this method to reduce the uncertainty and complexity of the problem. Based on the analysis of the temperature effect, the

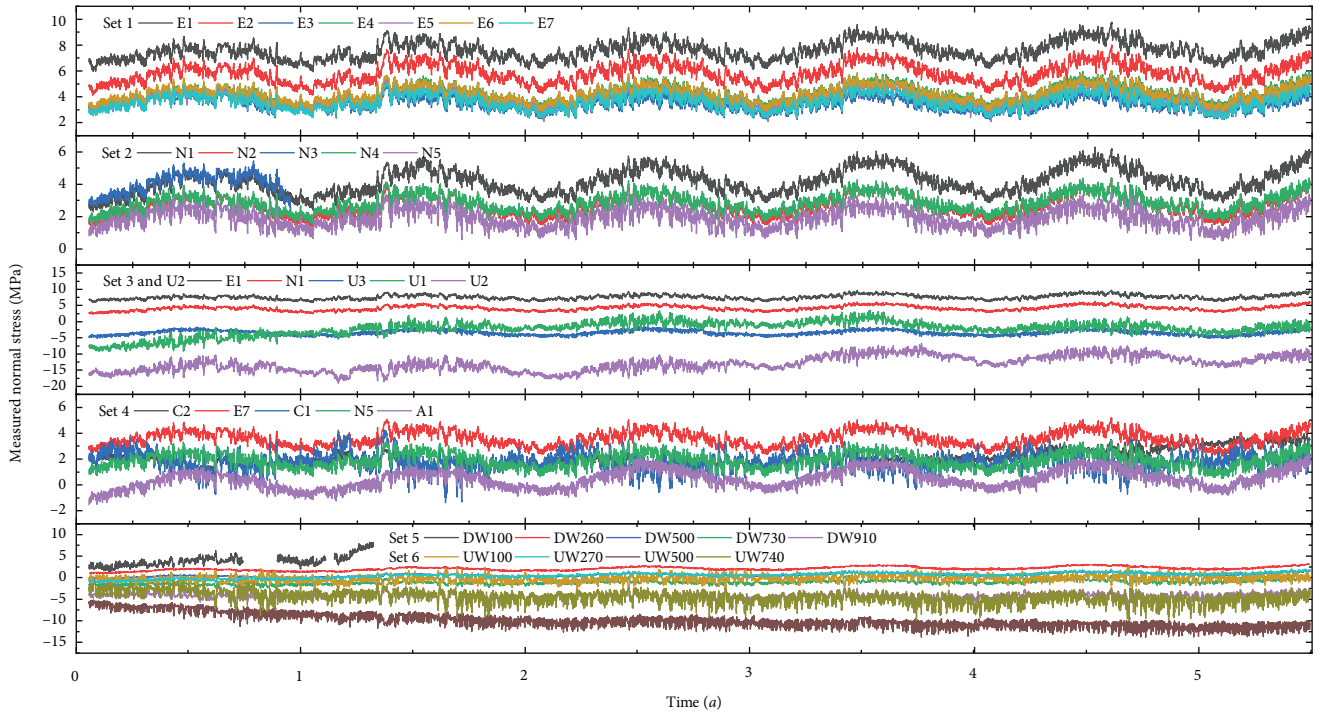

Figure 19: Time series of the measured normal stress in the cable–pylon anchorage zone.

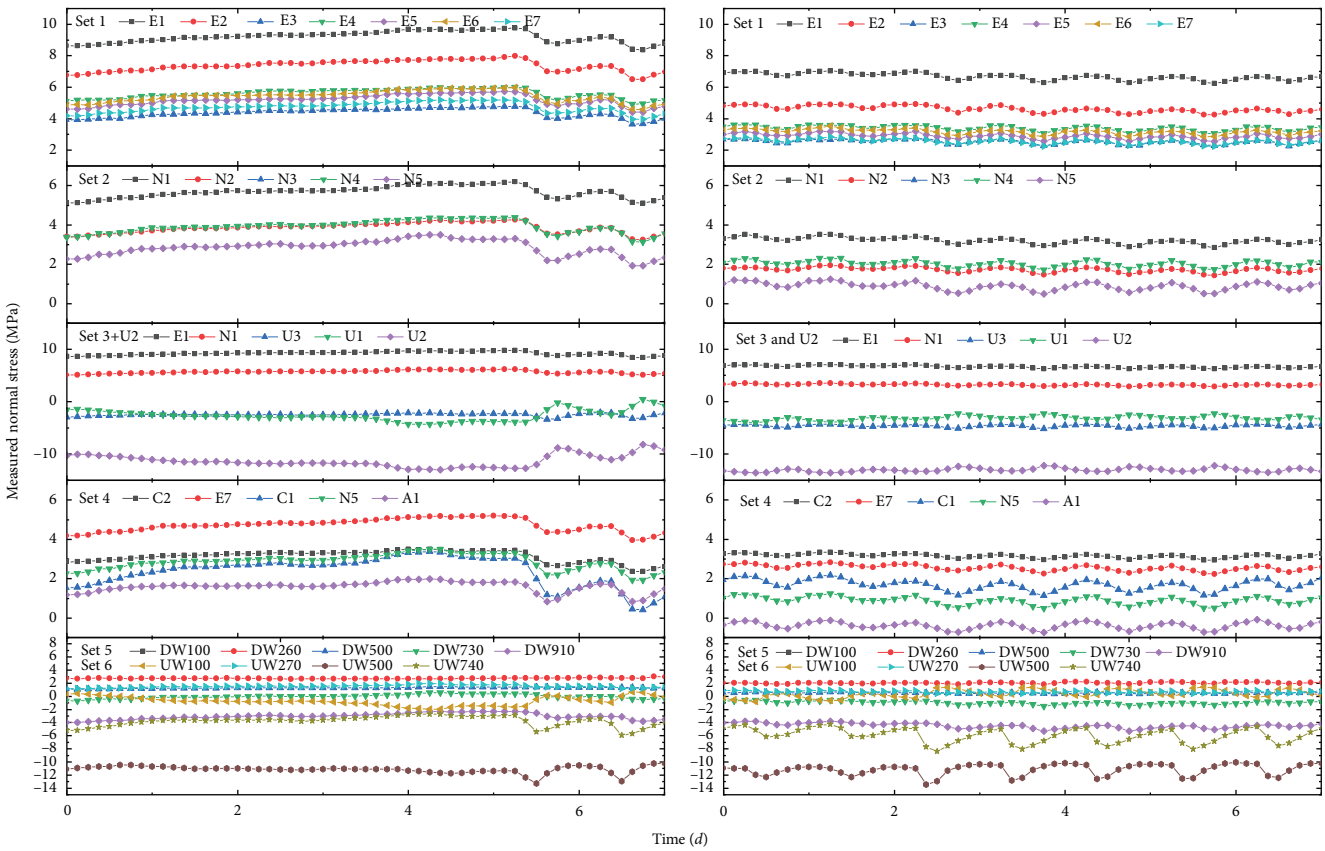

Figure 20: Stress variations on typical days.

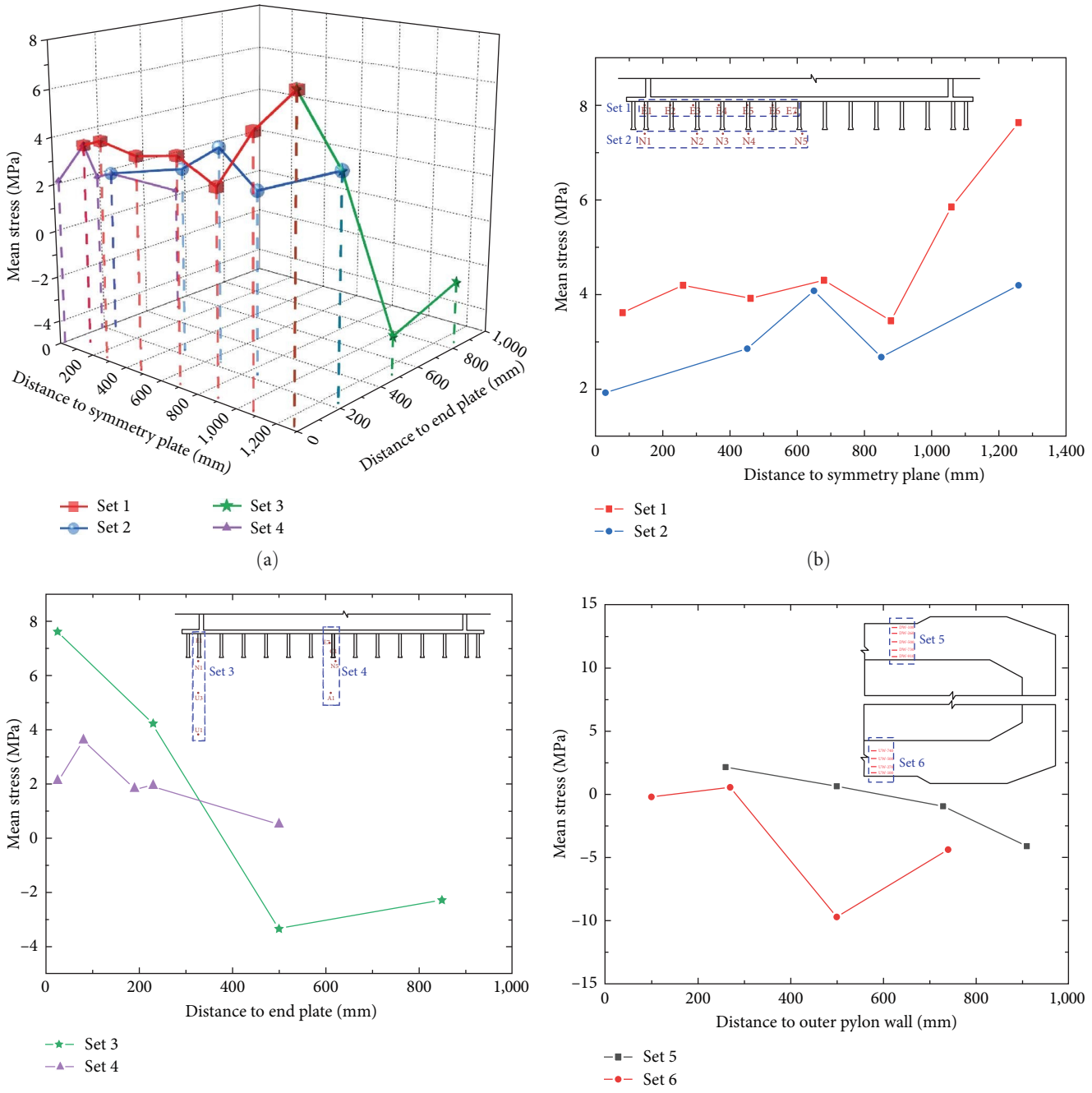

FIGURE 21: Relationship between the mean stress during operation and locations of monitoring points.

mechanical performance and structural safety of the cable–pylon anchorage zone can be analyzed more precisely. Because only 1 year data are used in this example, the effect of layered stripping is affected to some extent at both ends of the curve. However, this problem can be effectively solved if long-term monitoring data for a period longer than one year are used.

4. Stress Monitoring during Operation

The pylon concrete of the bridge is C50, and the elastic modulus $E = 3.5\times 10^4$ MPa. The designed compressive and tensile strength of C50 concrete are 23.1 and 1.89 MPa, respectively [32]. The elastic modulus can be considered approximately constant during the operating period. Therefore, the measured normal stress in the anchorage zone of the cable–pylon can be calculated by

$$\sigma = E \times \varepsilon = E \times G \times C(R_0 - R) + K(T_0 - T), \quad (6)$$

where ε is the measured concrete strain ($\mu\epsilon$, the pressure is positive, whereas the tension is negative), G is the standard

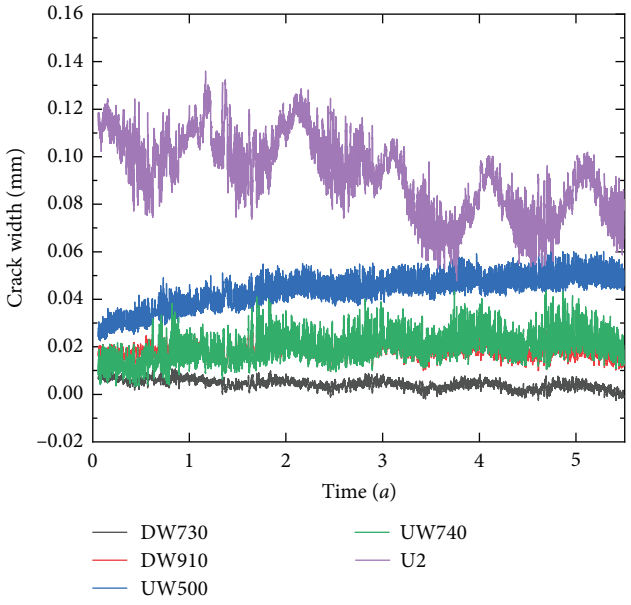

Figure 22: Time series variation of the crack width in the tensile zone.

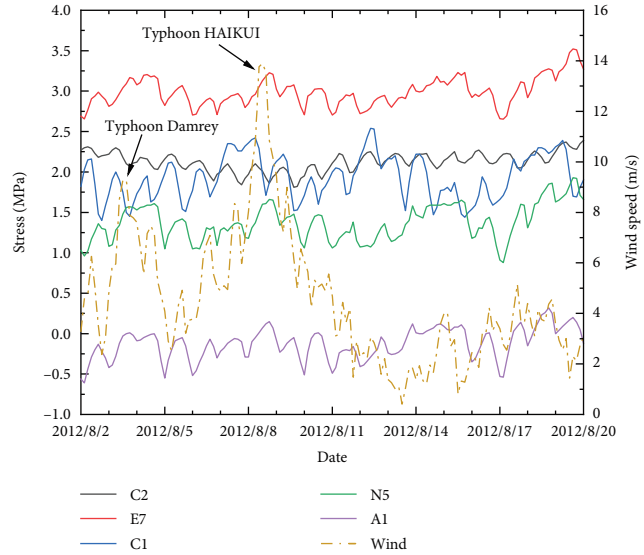

Figure 23: Wind speed and stress under the severe typhoon conditions.

coefficient of the concrete strain gauge (3.15), C is the calibration coefficient of the concrete strain gauge ($\mu\epsilon \times 10^{-3}\,\mathrm{Hz}^{-2}$), R_0 and R are the initial and current modules (Hz^2), T_0 and T are the initial and current temperatures (°C), and K is the temperature correction coefficient ($1.8\mu\epsilon/°\mathrm{C}$).

4.1. Analysis of The Results of Stress Monitoring. For convenience of the analysis, we define E1–E7 as Set 1, N1–N5 as Set 2, E1, N1, U3, and U1 as Set 3, C2, E7, C1, N5, and A1 as Set 4, DW100, DW260, DW500, DW730, and DW910 as Set 5, and UW100, UW270, UW500, and UW740 as Set 6. Equation 6 is used to calculate the measured normal stress in the anchorage zone of the cable–pylon during the operation period; its time series is shown in Figure 19. The stress variations in the cable–pylon anchorage zone during the cloudless period in summer and cold-wave period in winter are shown in Figure 20.

As shown in Figure 19, the stress monitoring results during the 5.5 years of operation are as follows: (1) the maximum compressive stresses of Sets 1–6 are 9.76 (E1), 6.19 (N1), 5.20 (E7), 3.14 (DW260), and 2.53 (UW100) MPa, respectively. The minimum compressive stresses of Sets 1 and 2 are 2.24 (E7) and 0.5 (N5) MPa, respectively; (2) the maximum tensile stresses of U1–U3 and Sets 4–6 are −9.15, −19.03, −5.16, −1.58 (A1), −6.82 (DW910), and −13.73 (UW500) MPa, respectively; (3) the maximum tensile stress of the longitudinal bridge on the sidewalls (upstream and downstream walls) of the pylon should be generated theoretically in summer.

According to Figure 20, the stress monitoring results show that (1) under sunny and cloudless conditions in summer, the stress variations in 1 day satisfy Set 1 ≈ Set 2, U1 ≈ U2 > U3 > E1 > N1 (Set 3 and U2), C1 > A1 > N5 > E7 > C2 (Set 4), and UW740 > UW500 > UW100 > DW910 > DW730 > DW260 ≈ UW270 > DW500 (Sets 5 and 6). (2) During the period of the continuous cooling of cold wave, the daily periodic variation in stress at each monitoring point is replaced by a monotonous trend variation. (3) The most adverse stress state in the compression zone appears in the early morning in winter, whereas the most adverse stress state in the tension zone appears in the afternoon in summer.

4.2. Stress Distribution at Different Locations. Because the monitoring points are basically arranged on the same horizontal plane, the stress distribution in the anchorage zone of the cable–pylon can be analyzed through the influence of the monitoring point positions on the stress. The locations of these monitoring points are shown in Table 1. The measured stress at each monitoring point in Figure 19 is averaged to obtain the relationship between the mean stress during operation and location of the monitoring point, as shown in Figure 21.

As shown in Figure 21, the mean stresses in Sets 1–6 satisfy E1 > E2 > E4 > E6 > E5 > E7 > E3, N1 > N3 > N4 > N2 > N5, E1 > N1 > U1 > U3, E7 > C2 > N5 > C1 > A1, DW260 > DW500 > DW730 > DW910, and UW270 > UW270 > UW740 > UW500, respectively. Figure 21(b) shows that the stress near the edge of the steel anchor box is larger than that near the axis of the bridge. Figure 21(c) shows that the vertical force changes from a compressive stress to a tensile stress in the longitudinal bridge direction from the inner wall to the outer wall. The vertical stress under the cable guide pipe is not higher than normal. Therefore, it is considered that the cable guide pipe is not in an unfavorable stress state. Figure 21(d) shows that the horizontal force changes from a compressive stress to a tensile stress in the transverse bridge direction from the outer wall to the inner wall in the cable–pylon anchorage zone; however, stress migration occurs in the upstream tower wall (Set 6).

4.3. Development of Cracks. As shown in Figure 19, the measured tensile stresses of DW730, DW910, UW500, UW740,

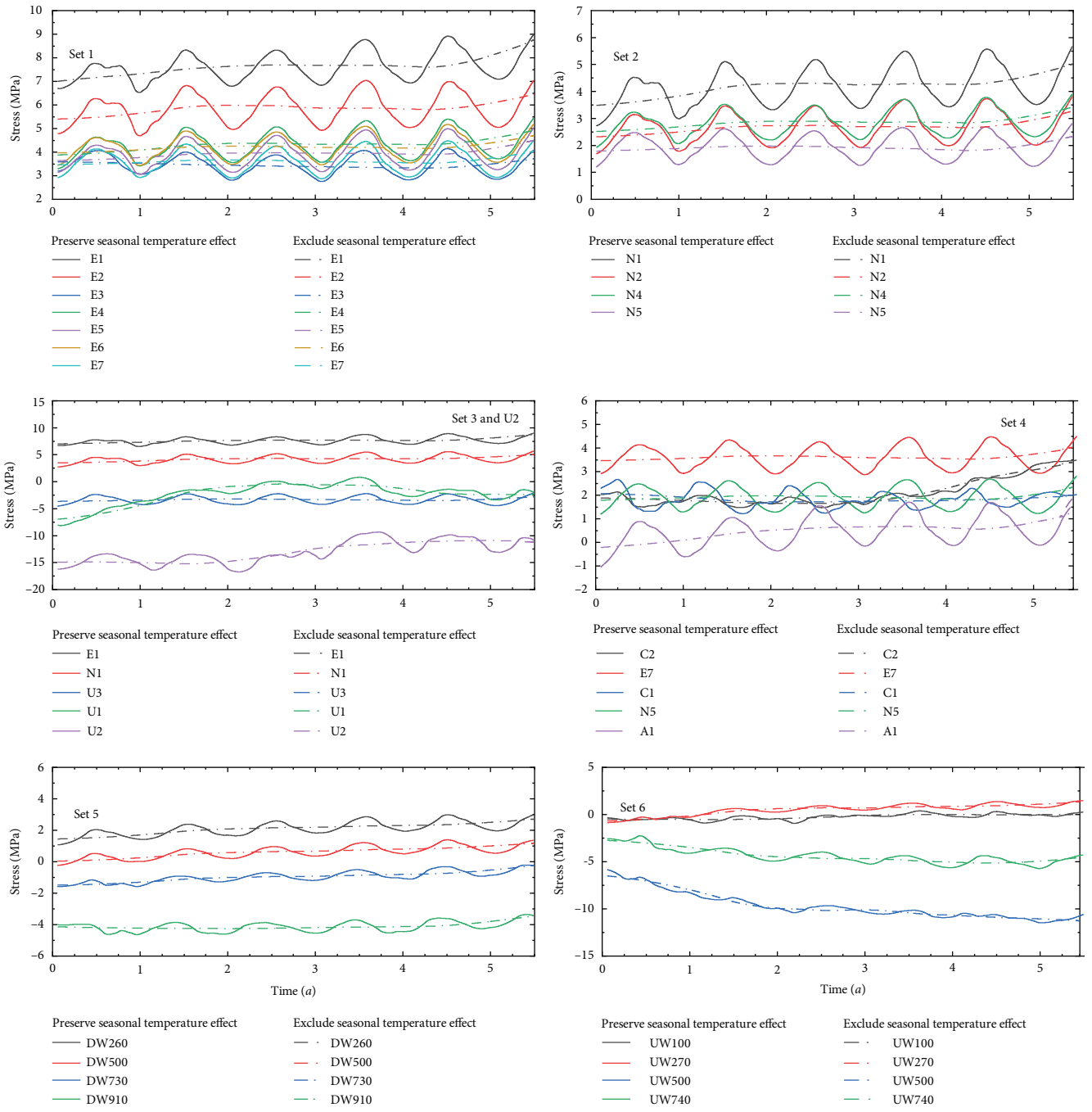

FIGURE 24: Stress changes in the anchorage zone after the stripping of short-term influencing factors.

and U2 exceed the designed tensile strength of C50 concrete (1.89 MPa), resulting in the cracking of the concrete. The time series variation in crack width is shown in Figure 22.

As shown in Figure 22, although the steel anchor box has a high-horizontal tensile strength and bears not less than 80% of the horizontal load, the tensile stress level of the top anchorage zone is still relatively high. During the operation period, the crack in the longitudinal pylon wall decreases slightly; however, the crack in the inner pylon wall of the transverse bridge still increases, and the concrete crack in the upstream pylon wall is more severe than that in the downstream pylon wall. The maximum crack widths of the upstream and downstream pylon walls are 0.03 and 0.06 mm, respectively.

4.4. Wind Effect. For a long-span cable-stayed bridge, the vibration of the cable structure is particularly prominent under the action of wind [33]. Taking Set 4 as an example, the monitoring data (2012/8/2 0:00–2012/8/20 0:00) under the severe typhoon conditions are selected to study the impact of wind speed on the stress in the cable–pylon anchorage zone, as shown in Figure 23. The instrument

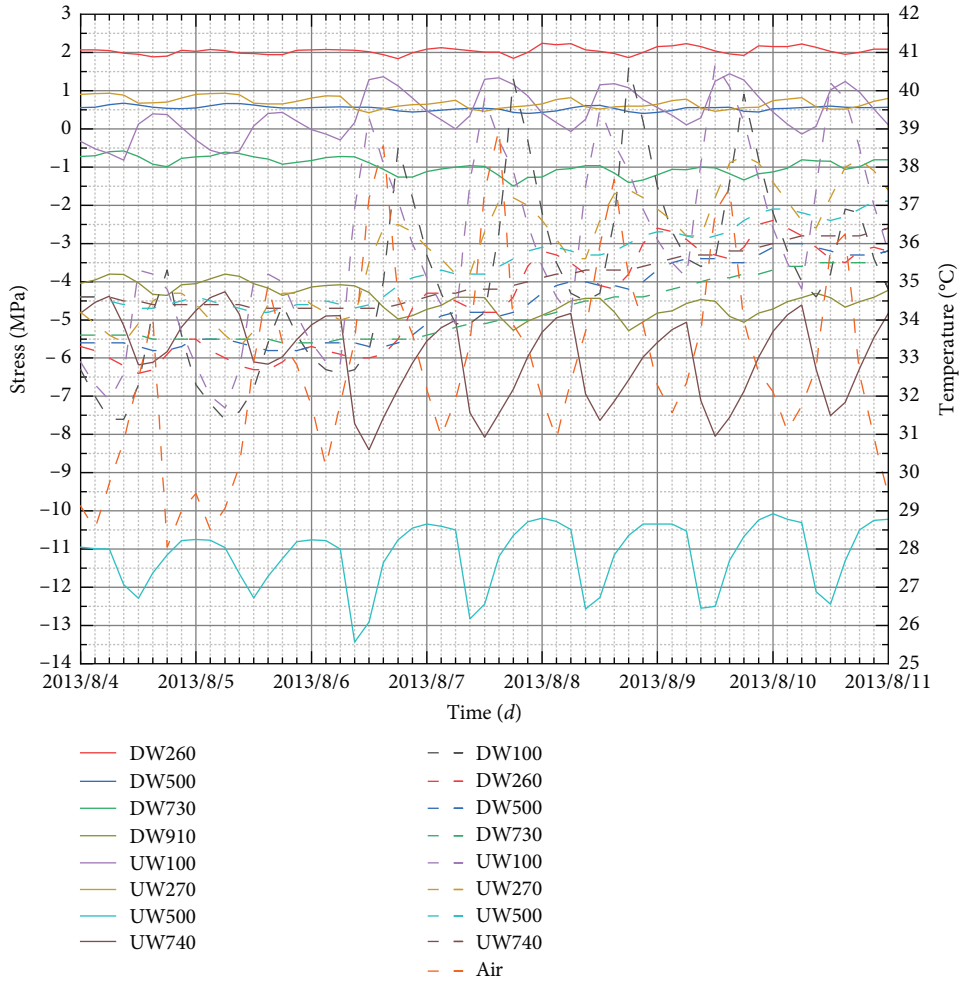

Figure 25: Diurnal periodic stresses and temperatures of the sidewall.

that collects wind speed data is located 10 m above the ground. As the elevation of the anchorage zone at the top of the cable–pylon is 295.5 m, the actual wind speed is higher than the measured value of the instrument, so the wind speed in Figure 23 is conservative.

As shown in Figure 23, there is no significant stress response in the anchorage zone even when the wind speed reaches 14 m/s, indicating that the stress in the anchorage zone is less affected by wind. The stress is highly correlated with the change of temperature, and the regular fluctuation proves that the influence of temperature on the stress in the anchorage zone is significant.

5. Analysis and Prediction of the Temperature Effect

Under normal conditions, the strain variation in the concrete structure caused by dead load can be regarded approximately constant, whereas the strain caused by concrete shrinkage and creep decays exponentially. The influence of the live load on the strain changes randomly, whereas the temperature strain exhibits an obvious periodicity and changes with the temperature.

5.1. Effect of Seasonal Temperature. Although the influence mechanism of the temperature on the concrete deformation is very complex, for a certain point, ignoring the more arbitrary change in temperature in the short period, the remaining part is the strain periodic term caused by the seasonal temperature change; the strain trend term is produced by long-term factors. The measured normal stress is investigated by a wavelet MRA. The stress of preserving the seasonal temperature effect and excluding the seasonal temperature effect obtained after layered stripping is shown in Figure 24.

As shown in Figure 24, during the operation period, (1) under the influence of seasonal temperature changes, the compressive stress changes to tensile from winter to summer, whereas the tensile stress changes to compressive from summer to winter, in accordance with the natural law of thermal expansion and cold contraction. (2) During the warming process from winter to summer, the vertical compressive stress of Sets 1–4 decreases by 1.0–2.1 MPa, whereas the horizontal tensile stress of Sets 5 and 6 increases by 0.4–1.5 MPa. (3) During the cooling process from summer to winter, the vertical compressive stress of Sets 1–4 increases by 0.4–2.3 MPa, whereas the horizontal tensile stress of Sets 5 and 6 decreases by 0.5–1.7 MPa. (4) Excluding the influence

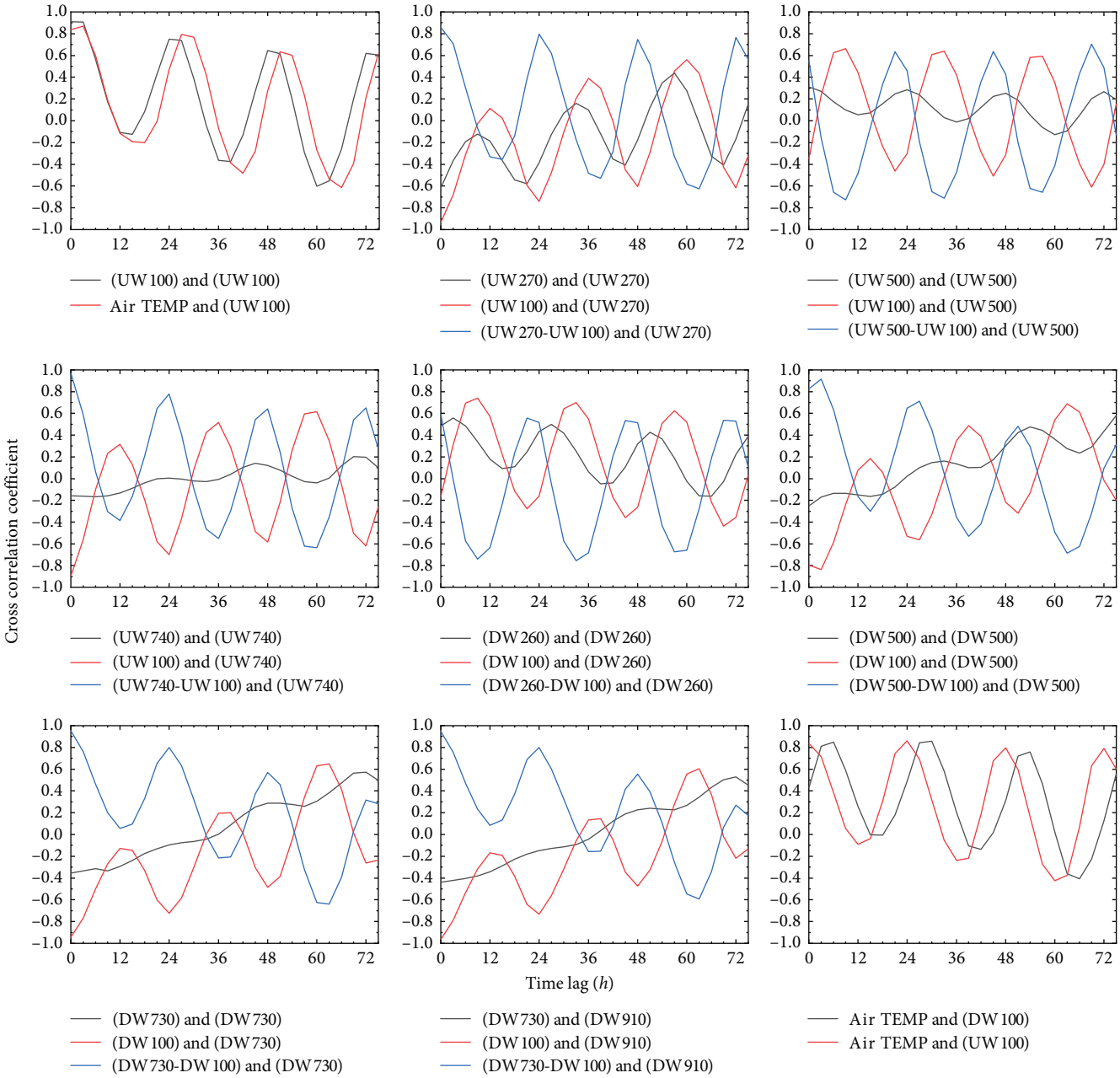

Figure 26: Cross-correlation function of monitoring points.

of seasonal temperature variations, the vertical compressive stress of Sets 1–4 increases by 0.1–5.1 MPa. In Sets 5 and 6, the stress at the other monitoring points does not change significantly, except that the tensile stress of UW740 is increased by 2.9 MPa and that of UW500 is increased by 5.2 MPa.

5.2. Effect of Daily Temperature. Because the stress state in the compression zone of the cable–pylon anchorage zone is relatively stable and does not change significantly in the short term, and the tension zone of the sidewall is strongly affected by the temperature effect, Sets 5 and 6 are selected as objects to study the influence of the daily temperature effect. Figure 25 shows the most adverse temperature effects for cloudless sunny days in summer (2013/8/4 0:00–2013/8/11 0:00).

As shown in Figure 25, both temperature and stress have a period of 24 hr. (1) Because the concrete heat transfer has a certain time lag and decreases exponentially, there is a nonlinear temperature in the pylon wall. (2) The changes in the measured temperature and stress are not synchronized, as well as the changes of concrete stress at different depths. From the outer wall to the inner wall, the time lag gradually increases. The trends of stress variations of the outer pylon wall and inner pylon wall are contrasting. (3) During the

Table 2: Parameters and coefficients of determination.

Monitoring point number	a_1	a_2	b	R^2
UW100	1.71	4.94	−222.4	0.847
UW270	0.73	−1.14	60.39	0.899
UW500	−8.27	0.40	−336.7	0.508
UW740	21.73	6.87	−397.5	0.959
DW260	2.39	1.28	14.9	0.705
DW500	0.85	−0.01	16.0	0.841
DW730	1.79	−1.04	10.2	0.923
DW910	1.60	−3.10	−17.7	0.939

diurnal cycle, the degree of influence of the temperature and change in stress satisfy outer wall > inner wall >1/2-thickness wall, unless there is a stress-transfer phenomenon.

5.3. Prediction of the Effect of Diurnal Temperature. To predict the daily temperature effect, the relationship between the temperature and daily thermal response should be studied quantitatively. The cross-correlation function between different variables can be obtained through a correlation analysis. The corresponding lag time can be determined according to the abscissa value of the first peak point of the cross-correlation function, which is helpful to understand the internal relationship between various variables. The results are shown in Figure 26. In the legend, the number of monitoring points in ( ) represents the temperature of the monitoring point or temperature difference between the monitoring points, whereas the number of monitoring points in [ ] represents the strain at the monitoring point.

As shown in Figure 26, as the depth of the concrete pylon wall increases, the influence of the temperature difference between sections begins to be larger than that of the temperature. The temperature difference between the inner and outer pylon walls is mainly controlled by the temperature of the outer pylon wall. Thus, the strain is highly correlated with the temperature of the outer pylon wall. Therefore, the regression model considering the measured temperature, pylon wall temperature difference, and time-lag effect can be expressed by

$$S = b + a_1 \times T_1(t - nk_1) + a_2 \times T_2 \times (t - nk_2), \quad (7)$$

where a_1, a_2, and b are the undetermined coefficients, S is the corresponding strain, T_1 and T_2 are the temperatures of the measuring points and temperature difference between the measuring points, respectively, and $nk_1$and nk_2 are the corresponding lag times.

Taking the monitoring data in Figure 25 as an example, the values of the undetermined parameters and determination coefficients in the regression model are listed in Table 2.

For a long-term monitoring, the parameter values in Table 2 change dynamically, however, this method is applicable to data at any time period under the daily cycle. Therefore, RMSE index can be used to quantitatively describe the accuracy of prediction and verify the validity of the model. The RMSE is defined as follows:

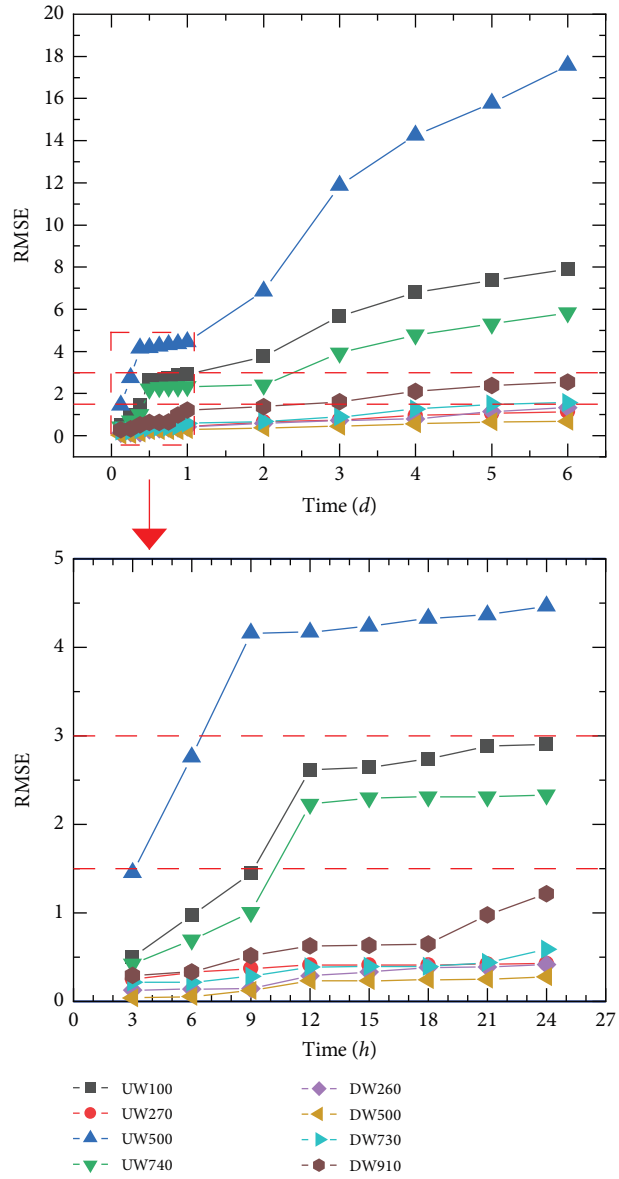

Figure 27: Relationship between the RMSE and predicted times.

$$RMSE = \sqrt{\frac{1}{N}\sum_{i=1}^{N}\left(X_i - \widehat{X}_i\right)^2}, \quad (8)$$

where X_i and $\widehat{X}_i$ are the measured and predicted values.

The change of the RMSE with predicted times are shown in Figure 27. The measured and predicted values are compared in Figures 28 and 29.

Figure 27 shows that the RMSE is highly correlated with the locations of the monitoring points. With the growth of the predicted times, the RMSE of UW270, DW260, DW500, DW730, and DW910 are always at a low level. When the prediction time exceeds one day, the RMSE of UW500, UW100, and UW740 increase rapidly. For monitoring points with large strain values, RMSE will also be higher than other monitoring points, so it can be specified that the

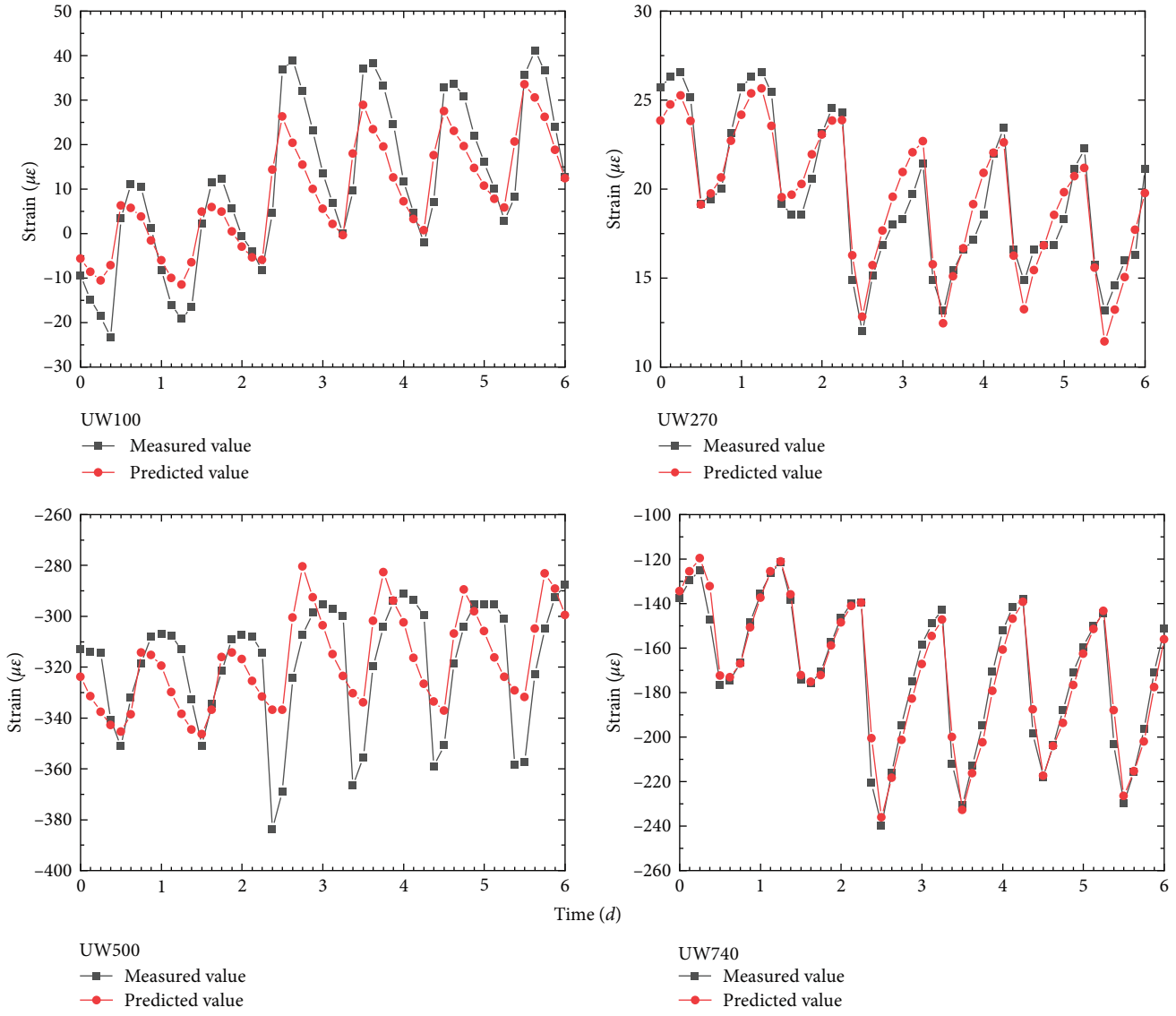

Figure 28: Measured and predicted values of the upstream pylon wall.

model has satisfactory accuracy when the RMSE is less than 1.5 or 3.

As shown in Figures 28 and 29, the prediction results of the model are satisfactory in most cases, particularly in the period when the temperature is stable, and the prediction is basically consistent with the measured curve. The prediction of the peak strain of the outer pylon wall is underestimated by the model, which may be due to the most intense solar radiation at this time and higher temperature variability. The cracking in UW500 is severe, which confirms that the existence of cracks significantly affects the prediction accuracy. Therefore, the degree of cracking at different positions of the structure can be estimated according to the accuracy of the prediction.

6. Conclusions

Based on the long-term SHM data of the cable–pylon anchorage zone, combined with the wavelet MRA and layered stripping method in this study, the separation of temperature effects at different scales was realized. The daily temperature effect was then predicted by a regression model, and structural status of the anchorage zone was evaluated during operation. The conclusions of this study can be summarised as follows.

(1) The measured maximum vertical compressive stress and horizontal tensile stress in the top anchorage zone were 9.76 and −19.03 MPa, respectively. The overall compressive stress level was low, whereas the tensile stress level was high. The stress near the edge of the steel anchor box was larger than that near the bridge axis. The cable guide pipe was not under an adverse stress.

(2) The horizontal tensile stress on the walls of the inner pylons in the upstream and downstream exceeded the tensile strength of the concrete, resulting in

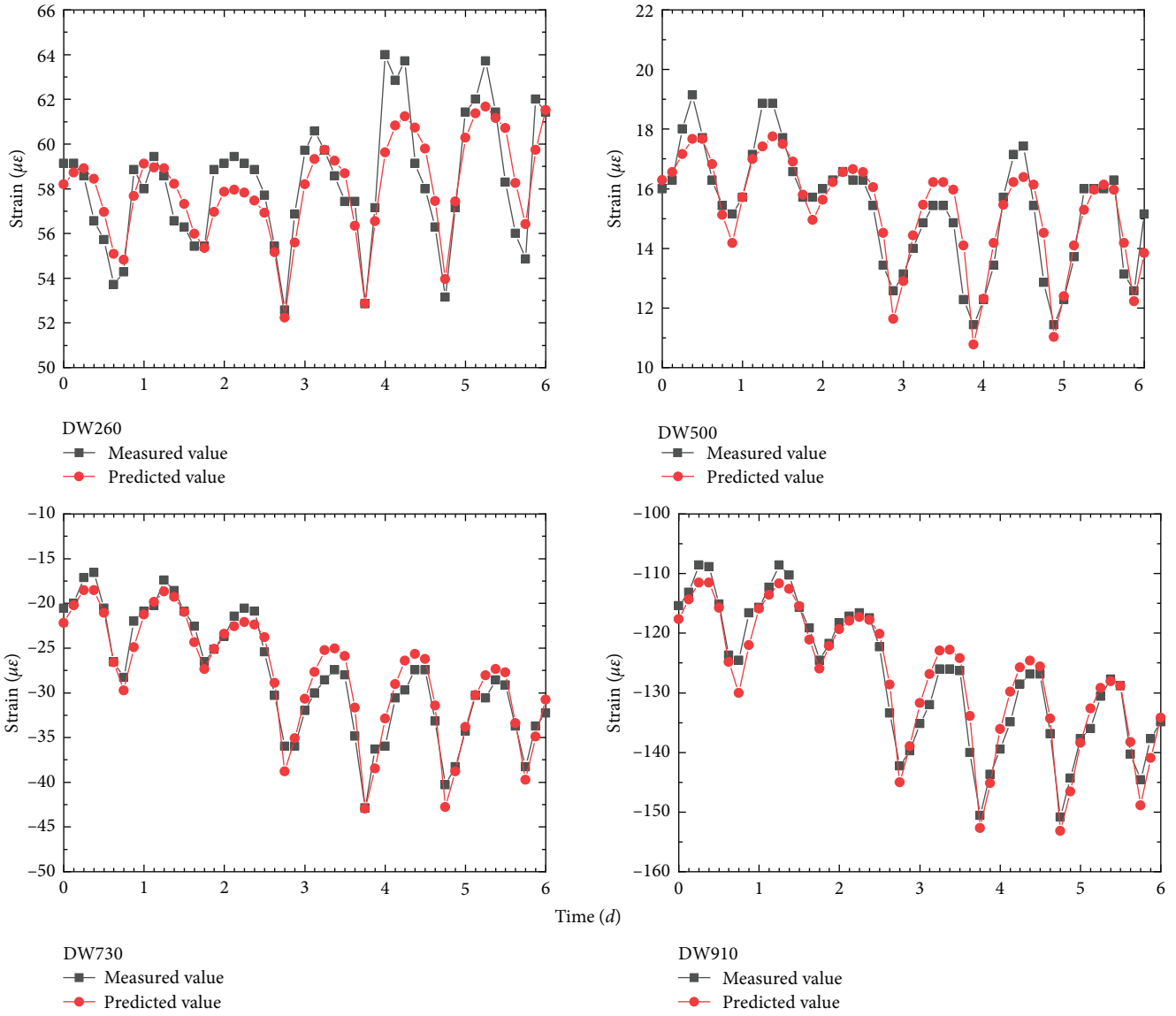

Figure 29: Measured and predicted values of the downstream pylon wall.

vertical tensile cracks with maximum widths of 0.03 and 0.06 mm, respectively. The width of the cracks increased gradually, whereas the stiffness of pylon wall decreased.

(3) The temperature was the main factor causing stress variations in the anchorage zone. The wavelet MRA and layered stripping method had good applicability and effectiveness in processing of long-term SHM data in the anchorage zone, which could be a foundation for the analysis of the temperature effect.

(4) Excluding the influence of the seasonal temperature, the compressive stress in the anchorage zone increased slightly. The horizontal tensile stress of the longitudinal bridge was reduced by 3.5 MPa; however, the horizontal tensile stress of the upstream pylon increased by 2.9–5.2 MPa. It is recommended to repair and maintain this area.

(5) The regression model that considered the measured temperature, section temperature difference and time lag effectively reflected the change trend of the daily thermal response. The model can predict the daily temperature effect at any time in the diurnal cycle. The accuracy of the model is reliable within 6 days, but for the location of severe cracks, the monitoring data should be updated in real time to ensure the accuracy.

Data Availability

The data supporting the current study are given in the article.

Conflicts of Interest

The authors declare that they have no conflicts of interest.

Acknowledgments

This work was supported by the "Jiangsu Province Policy Guidance Program (Industry-University-Research Cooperation)" (Project number: BY2015002-05).

References

[1] Q. T. Su, M. G. Zeng, and C. Wu, "Experiment study on steel-anchor-box of cable-pylon in Shanghai Yangtze River Bridge," *Engineering Mechanics*, vol. 25, no. 10, pp. 126–132, 2008.

[2] C. B. Luo, J. L. Zhou, W. Tian, and J. Dai, "Design and construction of Sutong Bridge tower," *Strategic Study of Chinese Academy of Engineering*, vol. 11, pp. 51–56, 2008.

[3] Q. T. Su and M. G. Zeng, "Analysis of mechanical behavior on concrete pylon steel-anchor-box in cable-stayed bridge," *Structural Engineers*, vol. 21, pp. 28–32, 2005.

[4] Y. B. Yang and Z. D. Lv, "A finite element method for vertical mechanics analysis of steel-concrete composite structure in pylon cable anchor zone of long span cable-stayed bridge," *Engineering Mechanics*, vol. 25, pp. 153–161, 2008.

[5] H. W. Ye, X. Xu, C. J. Li, and S. Z. Qiang, "Comparison of concrete cable-pylon anchorage models of long-span cable-stayed bridges," *Journal of Chongqing Jiaotong University (Natural Science)*, vol. 33, pp. 11–15, 2014.

[6] K. L. Chen, "Mechanical mechanism of the steel anchor housing in the anchorage zones of the cable pylons," *China Railway Science*, vol. 29, pp. 58–64, 2008.

[7] Q. T. Su and F. Qin, "Theory and experiment on horizontal mechanical behavior in anchorage zone of composite cable-pylon," *Journal of Tongji University (Natural Science)*, vol. 39, pp. 1120–1125, 2011.

[8] X. L. Yu and Q. Z. Zhang, "Analysis and test research on mechanical performance for steel-concrete composite anchor structure of cable-stayed bridge pylon," *Journal of Railway Science and Engineering*, vol. 6, pp. 16–20, 2009.

[9] L. F. Nie, X. G. Wang, J. Zhou, H. Wang, and J. H. Zeng, "Analysis of stress at anchoring zone of concrete tower considering temperature effect," *Highway*, vol. 4, pp. 110–114, 2019.

[10] Y. Li and Q. F. Cai, "Analysis of sunshine temperature effect of anchorage zone in concrete pylon of maling river bridge," *Bridge Construction*, vol. 42, pp. 48–53, 2012.

[11] Y. Li, S. H. He, and P. Liu, "Effect of solar temperature field on a sea-crossing cable-stayed bridge tower," *Advances in Structural Engineering*, vol. 22, no. 8, pp. 1867–1877, 2019.

[12] Q. W. Fan and Y. J. Qian, "Analysis of transient temperature gradient and thermal stress field of cable-stayed bridge tower by means of indirect coupling," *Journal of Shijiazhuang Railway Institute (Natural Science)*, vol. 21, pp. 18–22, 2008.

[13] Y. Zhou and L. M. Sun, "A comprehensive study of the thermal response of a long-span cable-stayed bridge: from monitoring phenomena to underlying mechanisms," *Mechanical Systems and Signal Processing*, vol. 124, pp. 330–348, 2019.

[14] H. Wang, Y. M. Zhang, J. X. Mao, H. P. Wan, T. Y. Tao, and Q. X. Zhu, "Modeling and forecasting of temperature-induced strain of a long-span bridge using an improved Bayesian dynamic linear model," *Engineering Structures*, vol. 192, pp. 220–232, 2019.

[15] T. Y. Tao, H. Wang, Q. X. Zhu, Z. Q. Zou, J. Li, and L. B. Wang, "Long-term temperature field of steel-box girder of a long-span bridge: measurement and simulation," *Engineering Structures*, vol. 236, Article ID 111924, 2021.

[16] Q. X. Zhu, H. Wang, J. X. Mao, J. Y. Min, J. R. Liu, and W. J. Wang, "Prediction of strain response of bridge under ambient excitation based on adaptive network-based fuzzy inference system," *China Journal of Highway and Transport*, vol. 32, pp. 62–70, 2019.

[17] J. H. Hu, L. H. Wang, X. P. Song, Z. H. Sun, J. F. Cui, and G. P. Huang, "Field monitoring and response characteristics of longitudinal movements of expansion joints in long-span suspension bridges," *Measurement*, vol. 162, Article ID 107933, 2020.

[18] D. Sen, K. Erazo, W. Zhang, S. Nagarajaiah, and L. M. Sun, "On the effectiveness of principal component analysis for decoupling structural damage and environmental effects in bridge structures," *Journal of Sound and Vibration*, vol. 457, pp. 280–298, 2019.

[19] H. Zhou, Y. L. Yi, Z. T. Ye, and M. Li, "Analysis of temperature filed and thermal effect in long-span composite girder cable-stayed bridge," *Bridge Construction*, vol. 50, pp. 50–55, 2020.

[20] D. H. Yang, T. H. Yi, H. N. Li, and Y. F. Zhang, "Monitoring and analysis of thermal effect on tower displacement in cable-stayed bridge," *Measurement*, vol. 115, pp. 249–257, 2018.

[21] X. Xu, Q. Huang, Y. Ren, D. Y. Zhao, J. Yang, and D. Y. Zhang, "Modeling and separation of thermal effects from cable-stayed bridge response," *Journal of Bridge Engineering*, vol. 24, no. 5, 2019.

[22] M. C. Jin, Z. R. Feng, J. B. Liu, and Z. J. Ye, "A study on temperature variation characteristics of tower cracks of cable-stayed bridge," *Highway*, vol. 1, pp. 39–42, 2010.

[23] R. Kromanis and P. Kripakaran, "Predicting thermal response of bridges using regression models derived from measurement histories," *Computers & Structures*, vol. 136, pp. 64–77, 2014.

[24] R. Kromanis and P. Kripakaran, "SHM of bridges: characterising thermal response and detecting anomaly events using a temperature-based measurement interpretation approach," *Journal of Civil Structural Health Monitoring*, vol. 6, no. 2, pp. 237–254, 2016.

[25] H. W. Zhao, Y. L. Ding, A. Q. Li, B. Chen, and K. P. Wang, "Digital modeling approach of distributional mapping from structural temperature field to temperature-induced strain feld for bridges," *Journal of Civil Structural Health Monitoring*, vol. 13, no. 1, pp. 251–267, 2023.

[26] B. J. Wu, Z. X. Li, T. H. T. Chan, and Y. Wang, "Multiscale features and information extraction of online strain for long-span bridges," *Smart Structures and Systems*, vol. 14, no. 4, pp. 679–697, 2014.

[27] X. Xu, Y. Ren, Q. Huang, D.-Y. Zhao, Z.-J. Tong, and W.-J. Chang, "Thermal response separation for bridge long-term monitoring systems using multi-resolution wavelet-based methodologies," *Journal of Civil Structural Health Monitoring*, vol. 10, no. 3, pp. 527–541, 2020.

[28] X. P. Wang, S. X. Huang, C. Kang, G. Q. Li, and C. F. Li, "Integration of wavelet denoising and HHT applied to the analysis of bridge dynamic characteristics," *Applied Sciences*, vol. 10, no. 10, Article ID 3605, 2020.

[29] Q. Huang, D. Y. Zhao, Y. Ren, and X. Xu, "Multiple time scale analysis of temperature-induced deflection of cable-stayed bridges," *Journal of Harbin Institute of Technology*, vol. 52, pp. 18–25, 2020.

[30] H. W. Zhao, Y. L. Ding, S. Nagarajaiah, and A. Q. Li, "Behavior analysis and early warning of girder deflections of a

steel-truss arch railway bridge under the effects of temperature and trains: case study," *Journal of Bridge Engineering*, vol. 24, no. 1, 2019.

[31] H. W. Zhao, Y. L. Ding, and A. Q. Li, "Representation of in-service performance for cable-stayed railway-highway combined bridges based on train-induced response's sensing data and knowledge," *Sensors*, vol. 22, no. 9, Article ID 3247, 2022.

[32] GB 50010-2010, Code for design of concrete structures.

[33] H. W. Zhao, Y. L. Ding, A. Q. Li, B. Chen, and X. N. Zhang, "State-monitoring for abnormal vibration of bridge cables focusing on non-stationary responses: from knowledge in phenomena to digital indicators," *Measurement*, vol. 205, Article ID 112148, 2022.